Materials Chemistry and Physics 359 (2026) 132480

Contents lists available at ScienceDirect

Materials Chemistry and Physics

journal homepage: www.elsevier.com/locate/matchemphys

Mixed glass former effect in tungsten-containing lithium borophosphate glasses: Spectroscopic structure–property correlations

Tomáš Hostinský [a,b,*], Grégory Tricot [c], Ladislav Koudelka [a], Petr Mošner [a], Lionel Montagne [d], Maksym Buryi [b], Andrey Prokhorov [e], Marta Razum [f], Luka Pavić [f], Ana Šantić [f]

[a] Department of General and Inorganic Chemistry, Faculty of Chemical Technology, University of Pardubice, 532 10, Pardubice, Czech Republic
[b] Institute of Plasma Physics of the Czech Academy of Sciences, U Slovanky 2525/1a, Prague 8, 182 00, Czech Republic
[c] Univ. Lille, CNRS, UMR 8516 – LASIRE - Laboratoire de Spectroscopie pour les Interactions, la Réactivité & l'Environnement F-59000 Lille, France
[d] University of Lille, CNRS, Centrale Lille, University of Artois, UMR 8181-UCCS-Unité de Catalyse et Chimie du Solide, F-59000, Lille, France
[e] FZU – Institute of Physics of the Czech Academy of Sciences, Na Slovance 1999/2, 182 00, Prague, Czech Republic
[f] Ruđer Bošković Institute, Bijenička cesta 54, 10000, Zagreb, Croatia

HIGHLIGHTS

- Mixed glass former effect studied by replacing P_2O_5 with B_2O_3 at constant Li_2O and WO_3.
- Advanced 1D/2D ^{11}B and ^{31}P MAS NMR revealed progressive phosphate depolymerisation.
- $^{[4]}B_3$ units act as network cross-linkers controlling thermal stability and network rigidity.
- Mixed glass former effect enchances DC conductivity by ~2 orders reaching 2.5×10^{-7} Ω^{-1} cm^{-1} at 30 °C.
- Results show strategy to optimise ionic transport in TMO-modified borophosphate glasses.

ARTICLE INFO

Keywords:
Borophosphate glasses
Glass properties
Glass structure
MAS NMR
Raman spectra
Ionic conductivity

ABSTRACT

The structure, thermal behaviour, and ionic conductivity of tungsten-containing lithium borophosphate glasses were investigated to study the interplay between mixed glass former effects and tungstate-modified phosphate networks. Glasses were prepared by systematically substituting P_2O_5 with B_2O_3 in the $40Li_2O–20WO_3–(40-x)P_2O_5–xB_2O_3$ system, while maintaining constant Li_2O and WO_3 contents in order to isolate the effect of mixed phosphate–borate glass formers. Thermal analysis revealed a pronounced mixed glass former effect, with the glass transition temperature (T_g) reaching a maximum at intermediate B_2O_3 content (15 mol%), followed by a gradual decrease at higher boron levels. Similar non-linear trends were observed for thermal stability ($T_c–T_g$) and the coefficient of thermal expansion, indicating optimal network connectivity at intermediate compositions. Raman spectroscopy combined with one- and two-dimensional ^{11}B and ^{31}P MAS NMR demonstrated that these trends originate from progressive phosphate network depolymerisation, changes in boron coordination from tetrahedral $^{[4]}B$ to trigonal $^{[3]}B$ units, and the formation of mixed P–O–B linkages at low-to-moderate B_2O_3 contents, whereas higher boron concentrations favour B–O–B connectivity and more open network motifs. Electrical conductivity measurements confirmed a positive mixed glass former effect, manifested as a non-linear enhancement of DC conductivity arising from phosphate–borate network reorganisation on a fixed tungstate-modified structural background. The DC conductivity increased by nearly two orders of magnitude, reaching a maximum of 2.49×10^{-7} Ω^{-1} cm^{-1} at 30 °C for x = 25 mol% B_2O_3, before slightly declining at higher boron contents. These results demonstrate that controlled introduction of a mixed glass former effect into a structurally optimised phosphate–tungstate network provides an effective strategy for further optimisation of ionic transport in lithium phosphate-based glasses.

* Corresponding author: Department of General and Inorganic Chemistry, Faculty of Chemical Technology, University of Pardubice, 532 10, Pardubice, Czech Republic.
E-mail address: tomas.hostinsky@upce.cz (T. Hostinský).

https://doi.org/10.1016/j.matchemphys.2026.132480
Received 4 December 2025; Received in revised form 24 March 2026; Accepted 1 April 2026
Available online 20 April 2026
0254-0584/© 2026 The Authors. Published by Elsevier B.V. This is an open access article under the CC BY license (http://creativecommons.org/licenses/by/4.0/).

1. Introduction

Lithium borophosphate glasses have been studied since the 1980s because of their pronounced changes in structural and physical properties upon network modification [1,2]. These systems contain two different glass formers, boron and phosphorus, within the glass network. The electrical conductivity of lithium borophosphate glasses depends not only on the Li^+ content but also on the ratio of the glass-forming oxides P_2O_5 and B_2O_3 [3]. The addition of B_2O_3 to lithium phosphate glasses not only reduces their hygroscopic nature but also enhances their thermal stability [4].

The introduction of boron oxide produces new linkages between phosphate chains through *P–O–*B bonds, whose amount increases with boron incorporation. Simultaneously, also a depolymerisation of the phosphate chains with Q^1 type phosphate units takes place. Room temperature electrical conductivity increases with boron content as well. Nevertheless, B_2O_3 contents higher than 20 mol% led to the crystallisation of Li_3PO_4 [5].

Two studies of lithium borophosphate glasses were carried out on the glasses of the composition $45Li_2O$-55 [xB_2O_3-(1-x)P_2O_5] prepared with the help of a hyper-fast quenching method allowing for the preparation of glasses containing more than 30 mol.% of boron oxide with a high degree of homogeneity [6,7]. The authors reported that their studied system exhibits the mixed glass former effect (MGFE) that is expressed through non-linear evolution of T_g and conductivity. The local and medium-range order was investigated by 1D/2D MAS-NMR [6]. Their study showed that the two distinct BO_4 signals were related to BO_4 attached to tetrahedral species (B or P) and BO_4 attached to at least one trigonal boron. The impact of MGFE on the evolution of T_g was explained by means of the network reticulation increase by the B–*O*–P bonds and the changes in conductivity were ascribed to be directly related to the number of tetra-coordinated boron species BO_4.

Another study of borophosphate glasses was realized by Muñoz et al., in 2017 [8] on the borophosphate glasses of the composition $50Li_2O$-xB_2O_3-(50-x)P_2O_5. Glasses were prepared by pouring the melt onto the brass moulds, and in this way homogeneous glasses were obtained for x = 0-20 mol% B_2O_3 and for x = 50 mol% B_2O_3. Both structural orders were probed using 1D- and 2D-correlation $^{11}B/^{31}P$ NMR experiments performed at very high magnetic field (18.8 T). The obtained data showed the presence of four borate and seven phosphate species and allowed estimating the number of *P–O–*P and *P–O–*B linkages.

In our previous work [9], we demonstrated that the incorporation of transition-metal oxides, specifically WO_3 and MoO_3, into lithium phosphate glasses leads to a pronounced increase in ionic conductivity, by approximately five and four orders of magnitude, respectively, while preserving their purely ionic transport character. This improvement was linked to systematic structural reorganisation of the phosphate network, driven by the formation of mixed phosphate–tungstate and phosphate–molybdate structural units that promote Li^+ mobility. Detailed ^{31}P MAS NMR and Raman spectroscopic analyses revealed that progressive substitution of P_2O_5 by WO_3/MoO_3 induces depolymerisation of the phosphate network and the formation of mixed Q^n_m species. Furthermore, that study highlighted the critical role of the modifier cation, showing that lithium-containing glasses exhibit higher ionic mobility and more favourable structure–property correlations than their sodium analogues. While these results established a clear structural origin for the exceptional ionic transport properties of WO_3/MoO_3-modified phosphate glasses, they were obtained in single-former phosphate networks and therefore did not address the potential role of mixed glass former effects.

Building upon this foundation, the present work extends the investigation to tungsten-containing mixed-former glass systems by introducing B_2O_3 into a structurally optimised lithium phosphate–tungstate network. Specifically, lithium borophosphate glasses were prepared by systematically substituting P_2O_5 with B_2O_3 in the $40Li_2O$–$20WO_3$–$40P_2O_5$ parent composition identified in the previous study. By keeping the Li_2O and WO_3 contents constant, the present compositional design isolates the effect of mixed glass formers (P_2O_5–B_2O_3) from changes in modifier concentration or tungstate content, allowing the mixed glass former effect to be probed under well-controlled conditions.

The structure of the resulting glasses was investigated using Raman spectroscopy and a comprehensive set of one- and two-dimensional MAS NMR experiments to elucidate changes in borate–phosphate connectivity and medium-range order, while impedance spectroscopy was employed to assess Li^+ ion transport. The primary objective of this study was to examine whether the controlled introduction of B_2O_3 into a tungstate-modified phosphate network enables further optimisation of ionic transport properties relative to the parent phosphate–tungstate glasses, through potential structural and transport synergies associated with mixed glass former effects, and to establish a direct structural basis for such behaviour.

2. Experimental

Glasses in the Li_2O–WO_3–P_2O_5–B_2O_3 system were prepared by melting Li_2CO_3 (99%), WO_3 (99.9%), H_3PO_4 (85 wt%, p. a.) and H_3BO_3 (99.5%) using a total batch weight of 25 g. The homogenised starting mixtures were heated at a rate of 5 °C·min^{-1} to 600 °C held at this temperature for 2 h to ensure complete dehydration and decomposition of precursors. Subsequently, the batches were heated to melting temperatures in the range of 1200–1350 °C, depending on composition, and held for 15–20 min under ambient air in a platinum crucible to achieve complete melting and homogenisation.

The melts were then poured onto a graphite mould preheated below the respective glass transition temperature ($T < T_g$) and allowed to cool to room temperature under ambient conditions. The weight of the glass sample, together with the remaining glass in the crucible, was more than 99 wt% and thus the weight loss was less than 1 wt%. We therefore considered the batch compositions as reflecting the actual compositions. The batch composition was verified using a density-based compositional consistency method, in which experimentally determined molar volumes were compared with additive-model predictions (details of the methodology and corresponding references are provided in the Supporting Information). The amorphous nature of the prepared glasses was verified by X-ray diffraction analysis (see Supporting Information).

The glass density, ρ, was determined using a helium gas pycnometer AccuPyc II 1340, where the volume of the sample was measured by calculating the volume of the helium gas displaced by the sample. The molar volume, V_M, was calculated using the expression $V_M = \overline{M}/\rho$, where $\overline{M}$ is the average molar weight of the glass composition $\overline{M} = a{\cdot}M(Li_2O) + b{\cdot}M(WO_3) + c{\cdot}M(P_2O_5) + d{\cdot}M(B_2O_3)$ calculated for $a + b + c + d = 1$. The oxygen packing density (OPD) was calculated as the number of oxygen atoms per unit volume of glass using the expression $OPD = n_O/V_M$, where n_O is the number of moles of oxygen atoms per mole of glass, determined from the glass composition according to $n_O = a{\cdot}(1) + b{\cdot}(3) + c{\cdot}(5) + d{\cdot}(3)$, corresponding to the oxygen content of Li_2O, WO_3, P_2O_5, and B_2O_3, respectively. The OPD values are expressed in units of mol O·cm^{-3}. The oxygen molar volume, V_O, defined as the molar volume per mole of oxygen atoms, was calculated as $V_O = V_M/n_O$, providing a complementary measure of the effective volume associated with oxygen in the glass network.

The thermal properties of the glasses were studied using a STA 449 F5 Jupiter (Netzsch) apparatus operating in DSC mode. DSC measurements were carried out at a heating rate of 10 °C·min^{-1} on powder samples (100 mg) prepared by milling bulk samples in a laboratory vibrational mill. The studied powder placed in Pt crucible with silica insert was heated under a flowing atmosphere of N_2. The thermal parameters were determined by evaluating the thermoanalytical DSC curves using Proteus Analysis (Netzsch) software. The glass transition

temperature (T_g) was identified as the onset of the first endothermic step, while the crystallisation temperature (T_c) was determined as the extrapolated onset point of the crystallisation peak. The glass transition temperature, dilatometric softening temperature and thermal expansion coefficient were determined from the dilatometric curves using the thermomechanical analyser Netzsch TMA 402. The coefficient of the thermal expansion, α, was determined as the mean value in a temperature range of 150-250 °C. The glass transition temperature, T_g, was determined from a change in the slope of the elongation versus the temperature plot and the dilatometric softening temperature, T_d, was obtained from the maximum of the expansion trace corresponding to the onset of viscous deformation under an applied load of 300 mN.

Electrical properties were measured on the ≈1 mm thick glass discs with gold electrodes, 6 mm in diameter, sputtered onto both sides using Sputter Coater SC7620. For the electrical characterization, complex impedance was measured in a frequency range from 0.01 Hz to 1 MHz at temperatures from −60 °C to 210 °C (temperature step: 30 °C). The temperature was controlled to an accuracy of ±0.2 °C.

Raman spectra in the range 1400-200 cm^{-1} were measured on glassy bulk and crystalline powder samples at a room temperature using a DXR Raman spectrometer Thermo Scientific with a 532 nm solid state (Nd: YAG) diode pumped laser.

^{31}P MAS NMR spectra were measured at 162.3 MHz using a BRUKER Avance 400 spectrometer with a 4 mm probe operating at a spinning frequency of 12.5 kHz. The acquisitions were recorded with 32 transients, a pulse length of 1.2 μs (π/4) and a recycle delay (rd) of 60 s, sufficient to enable full relaxation. The ^{11}B MAS NMR spectra were measured with a BRUKER Avance 800 spectrometer at 256.8 MHz with a 3.2 mm probe operating at a spinning frequency of 20 kHz. The acquisitions were recorded with 128 transients, a pulse length of 0.5 μs (π/12) and a recycle delay (rd) of 3 s, sufficient to enable full relaxation. The ^{31}P and ^{11}B chemical shift values are given relative to 85% H_3PO_4 and solid $NaBH_4$ at 0 and -42.06 ppm, respectively. The $^{11}B/^{31}P$ interactions were investigated with the ^{11}B (^{31}P) D-HMQC NMR experiments. The 2D maps were edited with π pulse lengths of 11 and 10 μs for ^{11}B and ^{31}P, respectively. The 2048 × 16 acquisition points were recorded under rotor-synchronized conditions with 256 transients and a rd of 3 s. The heteronuclear dipolar interaction was reintroduced with the application of a 2 × 0.5 s $SR4_1^2$ pulse scheme on the ^{31}P channel. The $^{11}B/^{11}B$ correlations were investigated with the ^{11}B DQ-SQ NMR sequence. The 8192 × 80 acquisition points were recorded with π pulse length of 11 μs, 128 transients and a rd of 3 s. The homonuclear dipolar interaction was reintroduced with the application of a 2 × 0.8 s $BR2_2^1$ pulse scheme.

Electron paramagnetic resonance (EPR) measurements were performed on a commercial Bruker ELEXSYS E580 X/Q-band spectrometer (X-band with a frequency of 9.4 GHz) with sensitivity of around 10^{12} spins/mT. The temperature range was 10–296 K (an Oxford Instruments ESR900 cryostat was used).

3. Results and discussion

3.1. General glass properties

Seven samples of the $40Li_2O–20WO_3–(40–x)P_2O_5–xB_2O_3$ (Series A) glass series were prepared using the melt-quenching technique described in the experimental section. Photographs of the obtained glasses are presented in Fig. 1. In this series, glassy samples were successfully obtained across the entire investigated B_2O_3 range (0–30 mol %). With further additions of B_2O_3 phase separation and crystallisation of the samples occur. In the studied glass series the samples exhibited a dark blue, transparent appearance at x = 0, which progressively deepened to an almost opaque black colour at x = 15. With further additions of B_2O_3, the intensity of the colour gradually diminished, resulting in a brown, transparent glass at x = 25, and a light brown, transparent appearance at x = 30. These colour changes are attributed to variations in the concentration of reduced tungsten species (W^{5+}) within the glass network (see EPR part). In addition to the $40Li_2O–20WO_3–(40–x)P_2O_5–xB_2O_3$ glass series discussed in this work, a complementary series containing 30 mol% WO_3, denoted as $40Li_2O–30WO_3–(30–x)P_2O_5–xB_2O_3$ (Series B), was also synthesized and characterized within the scope of this study. Although the present article focuses primarily on the 20 mol% WO_3 compositions, the data obtained for the 30 mol% WO_3 series were likewise evaluated and are included both in the Supporting Information and in the comparative discussion of the electrical properties to illustrate the influence of WO_3 content on ionic conductivity.

Key physico-chemical properties, including density (ρ), molar volume (V_M), oxygen packing density (OPD), oxygen molar volume (V_O), glass transition temperature (T_g), crystallisation temperature (T_c), thermal stability ($T_c–T_g$), dilatometric softening temperature (T_d), and the coefficient of thermal expansion (α), are summarised in Table 1.

The compositional dependence of density and molar volume for the studied glasses is illustrated in Fig. 2 (left panel). Substitution of P_2O_5 by B_2O_3 results in a systematic decrease of the molar volume from 35.4 to 26.9 $cm^3\ mol^{-1}$ (Table 1), accompanied by a gradual increase in density. Although B_2O_3 has a lower molar mass than P_2O_5, the pronounced contraction of the glass network (decreasing V_M) outweighs the mass effect and leads to overall densification. This behaviour indicates that the density evolution in the present glass series is governed primarily by structural compaction rather than by the incorporation of heavier constituent oxides.

To further quantify changes in glass compactness, oxygen packing density (OPD) and oxygen molar volume (V_O) was calculated and values are presented in Fig. 2 (right panel) and summarised in Table 1. OPD increases from 0.084 to 0.089 mol O·cm^{-3} with increasing B_2O_3 content, while V_O decreases from 11.8 to 11.2 cm^1 mol O^{-1}. The trends show that the oxygen sublattice becomes progressively more densely packed as P_2O_5 is replaced by B_2O_3, with the most pronounced changes occurring up to compositions x ≤ 20 mol% B_2O_3, at higher B_2O_3 contents (x = 20–30 mol%), OPD and V_O approach a near-plateau, suggesting that further substitution produces only minor additional compaction, which is consistent with the more gradual evolution of density observed at x ≥ 20 mol% B_2O_3.

From a structural perspective, this non-linear behaviour can be explained by changes in boron coordination within the glass network. At low B_2O_3 concentrations, the formation of tetrahedrally coordinated BO_4 units is favoured, particularly in the presence of lithium cations, which are known to stabilise fourfold-coordinated boron [10,11]. The increased fraction of BO_4 units and the associated formation of mixed

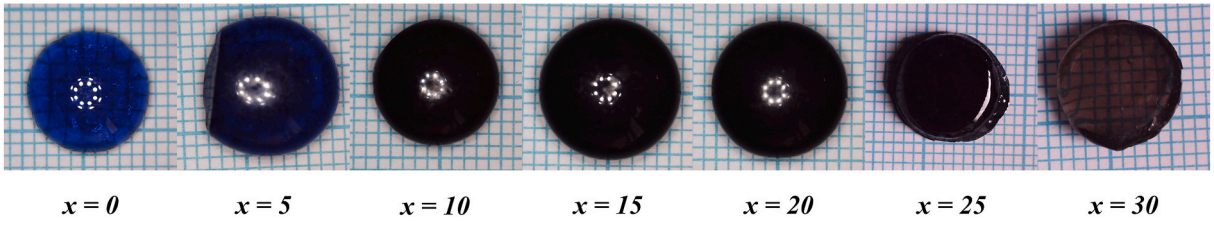

Fig. 1. Glass samples of the $40Li_2O–20WO_3–(40–x)P_2O_5–xB_2O_3$ series (the dots visible on the sample x = 0−20 are the reflection of the LED of the used digital microscope).

Table 1
Composition, density, ρ, molar volume, V_M, glass transition temperature[a], T_g, crystallisation temperature, T_c, glass thermal stability parameter, T_c-T_g, dilatometric softening temperature, T_d, and the coefficient of thermal expansion, α, of $40Li_2O–20WO_3–(40–x)P_2O_5–xB_2O_3$ glass series.

Li_2O	P_2O_5	WO_3	B_2O_3	ρ±0.02	V_M±0.5	OPD ±0.001	V_O±0.2	T_g±2[a]	T_c±2	T_c-T_g	T_d±1	α±0.5
batch/mol%				g cm^{-3}	cm^3 mol^{-1}	mol O cm^{-3}	cm^3 mol O^{-1}	°C				ppm/°C
40	40	20	0	3.25	35.4	0.0848	11.8	386 (387)	-	-	405	16.8
40	35	20	5	3.33	33.5	0.0866	11.6	404 (404)	-	-	423	14.6
40	30	20	10	3.38	31.9	0.0878	11.4	443 (440)	-	-	462	14.4
40	25	20	15	3.43	30.4	0.0888	11.3	448 (449)	631	183	466	13.2
40	20	20	20	3.45	29.2	0.0890	11.2	447 (445)	572	125	459	13.9
40	15	20	25	3.46	28.0	0.0893	11.2	431 (430)	533	102	444	14.9
40	10	20	30	3.47	26.9	0.0892	11.2	423 (421)	502	79	436	15.6

[a] Glass transition temperature obtained from TMA curve. Data obtained from DSC in brackets.

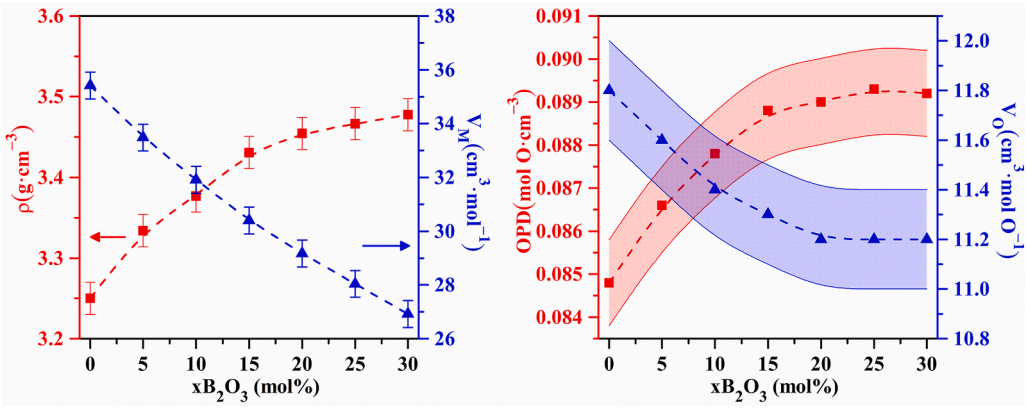

Fig. 2. Density and molar volume (left panel) and oxygen packing density and oxygen molar volume (right panel) of the $40Li_2O–20WO_3–(40–x)P_2O_5–xB_2O_3$ glass series (dashed lines are only a guide to the eye). In the right panel, shaded regions around the curves represent the uncertainty, shown instead of conventional error bars for improved visual clarity.

B–O–P linkages promote more efficient space filling and enhanced network connectivity, consistent with the strong reduction of V_M and V_O at $x \leq 20$ mol% B_2O_3. With further B_2O_3 additions, the prevalence of trigonal BO_3 units is expected, which is expected to moderate further densification and is consistent with the near-plateau in OPD and V_O at high borate levels. This structural evolution is examined in detail in the following section using ^{11}B MAS NMR spectroscopy.

3.2. *Thermal behaviour of glasses*

The DSC curves of the $40Li_2O–20WO_3–(40–x)P_2O_5–xB_2O_3$ glass series are presented in Fig. 3. In this figure endothermic events corresponding to the glass transition temperature (T_g) are observed, followed in some compositions by exothermic peaks of crystallisation, followed by an additional endothermic signal, corresponding to the melting of the crystallised phase. It should be noted, however, that the absence of a crystallisation peak in a DSC trace does not necessarily imply that the glass is fully amorphous or completely resistant to crystallisation. Rather, it may reflect that the applied experimental conditions, particularly the heating rate of 10 K min^{-1} used in this study, was not sufficient to trigger detectable crystallisation events within the temperature window of the measurement. The values of T_g, the crystallisation temperature (T_c), and the thermal stability parameter (T_c-T_g) are summarised in Table 1. For compositions with $x \leq 10$, no crystallisation peak is detected under the applied DSC conditions, and T_c (and consequently $T_c–T_g$) is therefore not defined; these cases are marked as "-" in Table 1.

Glass transition temperature increases in these glasses from 386 °C at $x = 0$ to a maximum of 448 °C at $x = 15$ mol% B_2O_3, beyond which it slightly decreases to 423 °C at $x = 30$. This non-monotonic trend suggests that the initial incorporation of B_2O_3 leads to enhanced network connectivity, associated with the formation of B–O–P linkages and

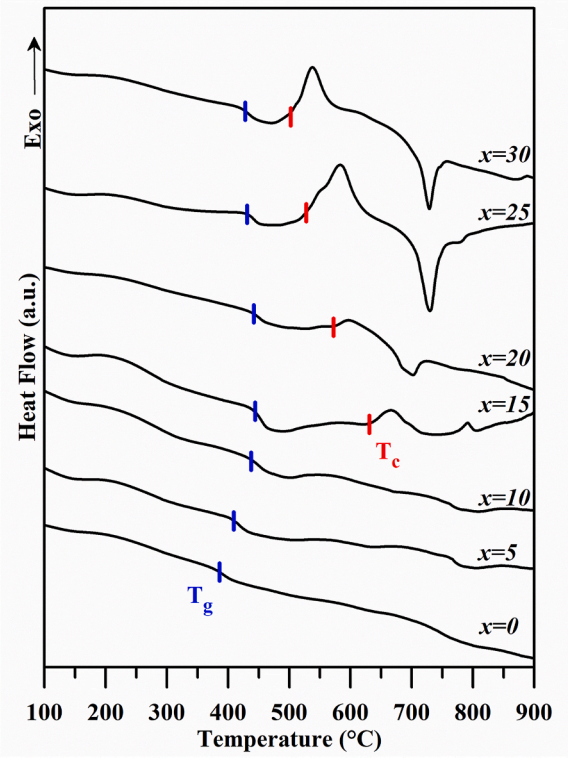

Fig. 3. DSC curves of the $40Li_2O–20WO_3–(40–x)P_2O_5–xB_2O_3$ glass series.

tetrahedrally coordinated boron species, resulting in a more cross-linked and rigid glass structure. At higher B_2O_3 contents, the observed decrease in T_g indicates a progressive reduction in network connectivity, which is commonly associated with a shift towards lower-coordinated boron environments and increased borate–borate interactions, as confirmed by the spectroscopic analyses discussed later in the manuscript. A similar evolution is observed for the crystallisation temperature (T_c), which reaches a maximum of 631 °C at x = 15, then gradually decreases. The thermal stability parameter $T_c - T_g$ (for the composition where it could be evaluated) also follows this trend, peaking at 183 °C, indicating that the resistance of the glass to devitrification is the highest at intermediate B_2O_3 contents. For compositions where no crystallisation peak is detected within the experimental window ($x \leq 10$), T_c and T_c–T_g are not defined and are therefore excluded from the discussion of thermal stability based on this parameter.

The glass transition temperatures (T_g), along with the dilatometric softening temperatures (T_d) and coefficients of thermal expansion (CTE), were also determined from thermomechanical analysis (TMA) and are presented in Fig. 4 and Table 1. The evolution of T_d closely mirrors that of T_g. The T_g values obtained from TMA are considered more representative of the bulk glass behaviour and less dependent on subjective baseline evaluation than DSC-derived values; therefore, they are used for quantitative comparison throughout this work. The coefficient of thermal expansion (CTE), which provides a sensitive measure of network connectivity and compactness, shows a decreasing trend with increasing B_2O_3 content in both series up to intermediate compositions. In this glass series CTE drops from 16.8 to a minimum of 13.2 ppm °C^{-1} at x = 15, indicating enhanced structural rigidity, and then increases again with further B_2O_3 additions. The evolution is probably caused by the increased occurrence of BO_3 structural units and their mutual linking by homopolar B–O–B bonds. These observations reinforce the interpretation that the maximum network cross-linking occurs at intermediate B_2O_3 levels (x = 15), beyond which the prevalence of non-bridging oxygens and BO_3 units causes a relaxation of the glass structure.

Thus, the thermal behaviour of this glass series is strongly governed by the interplay between phosphate, tungstate, and borate structural units. The formation of mixed linkages such as P–O–B and possibly also B–O–W enhances thermal stability and structural compactness up to a critical B_2O_3 concentration, while excessive boron incorporation promotes the formation of more open network features that reduce the thermal stability.

3.3. Structural analysis by Raman spectroscopy

The Raman spectra of the glass series $40Li_2O–20WO_3–(40–x)P_2O_5–xB_2O_3$ are depicted in Fig. 5 and reveal bands associated with phosphate, tungstate, and borate structural units. In the parent boron-free composition (x = 0), the phosphate network displays a broad band at approximately 1161 cm^{-1}, commonly attributed to the symmetric stretching vibrations of non-bridging and bridging oxygen atoms in Q^2 units [12]. Although this band lies in the spectral region typically associated with metaphosphate units, the effective modification state of the phosphate sub-network cannot be directly inferred from the nominal O/P ratio (x = 0; O/P = 3.75), as a fraction of Li_2O also participates in the modification and charge compensation of tungstate units, as indicated by the ν_s (W–O$^-$) Raman band.

Accordingly, the phosphate network at x = 0 is best described as consisting of Q^2-type chain segments coexisting with more polymerised phosphate-tungstate species, rather than a purely metaphosphate structure. With increasing B_2O_3 content, the gradual decrease and eventual disappearance of the ν_s (P=O) band in the 1215–1256 cm^{-1} range, together with the emergence of a distinct band near 1133 cm^{-1} assigned to Q^1 units [12], indicate a progressive depolymerisation of the phosphate sub-network. These trends are consistent with the structural evolution inferred from ^{31}P MAS NMR spectroscopy.

At x = 0, the Raman spectrum in the 600–800 cm^{-1} region is dominated by a broad band centred at ~700–707 cm^{-1}, which is assigned to the symmetric P–O–P stretching vibration of Q^2 phosphate units [12–14]. A weak high-frequency shoulder near ~730 cm^{-1} is consistent with a minor contribution from ν_s (P–O–P) (Q^1) environments, in agreement with the low expected fraction of Q^1 species in the parent composition and with reference spectra of pyrophosphate glasses [12]. In addition, a weak feature is observed near ~633 cm^{-1}, however, its origin cannot be uniquely established, and it is therefore left

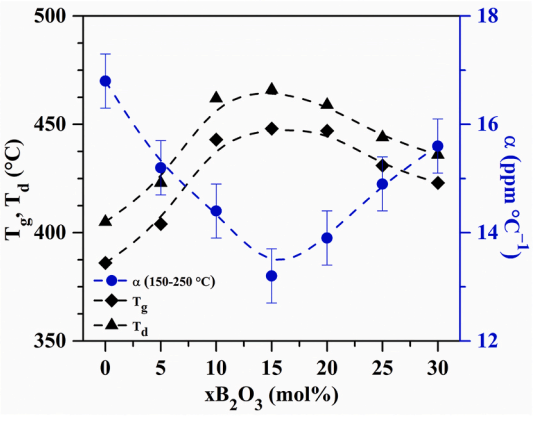

Fig. 4. Compositional dependence of glass transition temperature T_g, dilatometric softening temperature, T_d, and coefficient of thermal expansion, α, in the glass series $40Li_2O–20WO_3–(40–x)P_2O_5–xB_2O_3$ glass series obtained from TMA (dashed lines are only a guide to the eye).

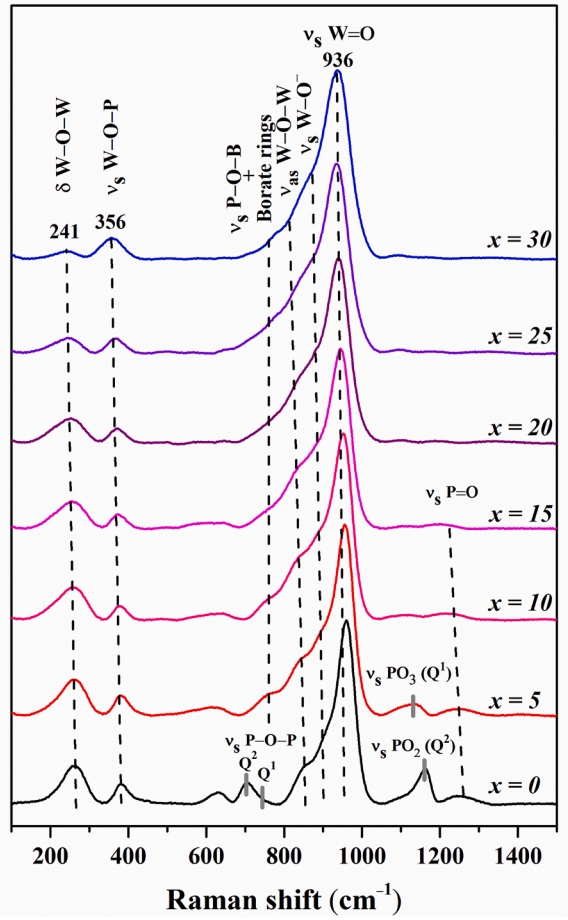

Fig. 5. Raman spectra of the $40Li_2O–20WO_3–(40–x)P_2O_5–xB_2O_3$ glass series.

unassigned. With increasing B_2O_3 content, the phosphate-related Raman bands progressively decrease in intensity, consistent with dilution and depolymerisation of the phosphate sub-network.

An intense band at 936–937 cm^{-1}, attributed to the symmetric stretching vibrations of terminal W═O bonds in WO_6 octahedra [15,16], accompanied by a shoulder at slightly lower wavenumbers, associated with W–O^- bond vibrations within the same units [15,16]. The invariant position of this band across both series implies that the geometry and coordination of the tungsten units remains unchanged, preserving their octahedral environment throughout the compositional range.

A broad underlying envelope between 820 and 850 cm^{-1} is evident in both series, arising from the stretching vibrations of W–O–W bridges in three-dimensional WO_6 clusters [15,16]. A shoulder following band around 800 cm^{-1} emerges in this glass series, increasing in intensity with B_2O_3 content. This band is attributed to P–O–B stretching vibrations [17–19] and possibly also to symmetric modes of borate ring structures [18,19], indicating the incorporation of boron into the glass network and the formation of mixed phosphate-borate linkages.

At lower wavenumbers Raman spectra exhibit characteristic metal–oxygen vibrations: a broad band at approximately 250 cm^{-1}, attributed to W–O–W bending modes, and another in region of 340-370 cm^{-1}, assigned to W–O–P bending vibrations. These bands provide further evidence of the presence mixed phosphate-tungstate units and their integration into the phosphate glass matrix.

Raman spectra reveal that increasing B_2O_3 content induces progressive depolymerisation of the phosphate network, formation of P–O–B linkages, and possibly increased clustering of WO_6 units.

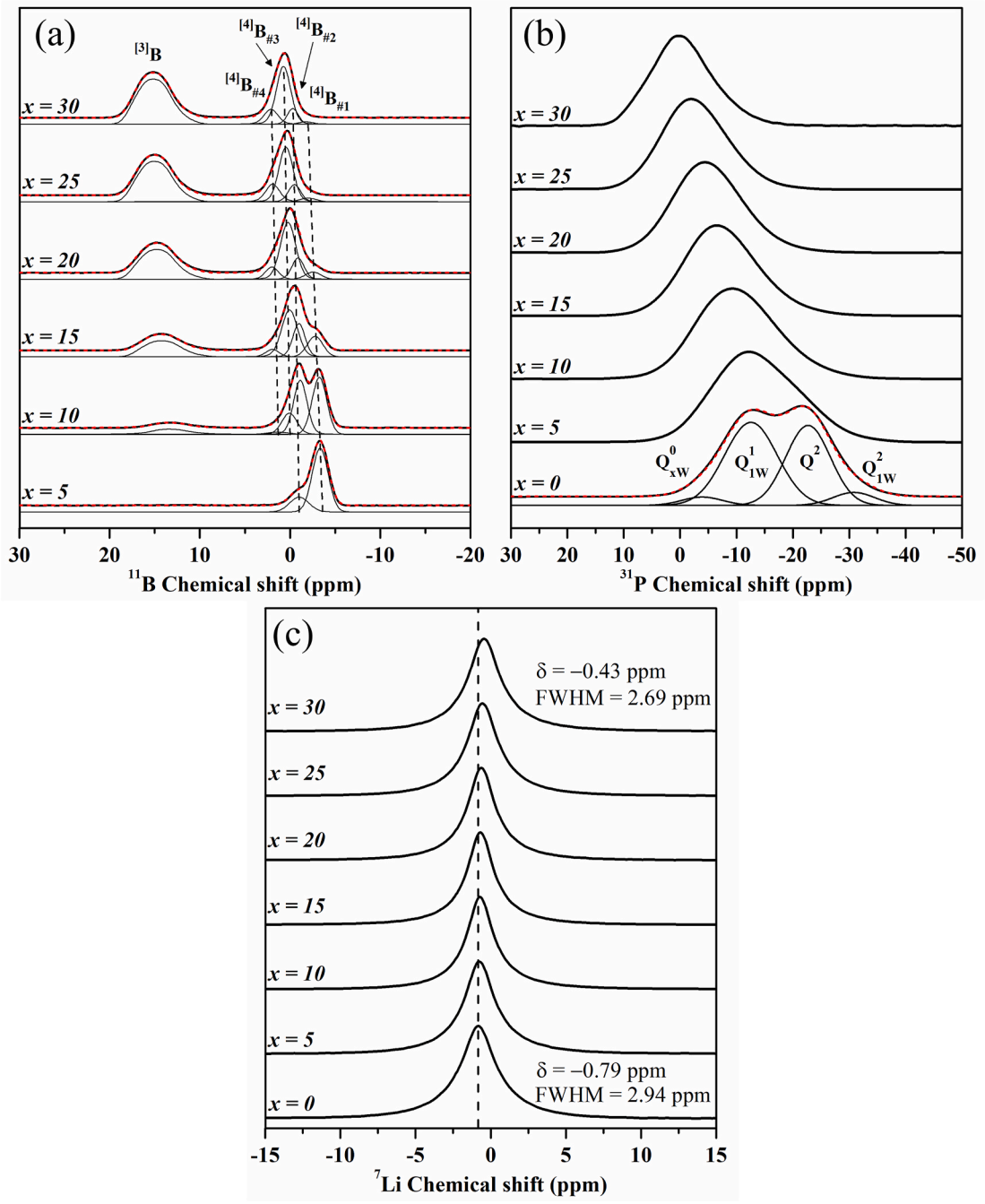

Fig. 6. 1D^{11}B MAS NMR (a), 1D^{31}P MAS NMR (b) and 1D ^{7}Li MAS NMR (c) spectra accompanied with representative decomposition of the $40Li_2O–20WO_3–(40–x)P_2O_5–xB_2O_3$ glass series.

Although the Raman spectra provide valuable information on tungstate structural units, they offer limited insight into the detailed structural characteristics of phosphate and borate domains. Therefore, further structural investigations using MAS NMR spectroscopy were undertaken to obtain a more comprehensive understanding of the local environments of phosphorus and boron species.

3.4. Structural analysis by 1D/2D MAS NMR spectroscopy

3.4.1. 1D MAS NMR characterization

The 1D ^{31}P, ^{11}B, and ^{7}Li MAS NMR spectra of the $40Li_2O–20WO_3–(40–x)P_2O_5–xB_2O_3$ borophosphate glass series are presented in Fig. 6. The high-field ^{11}B MAS NMR spectra (Fig. 6a) allow for clear differentiation between trigonal [3]B and tetrahedral [4]B units, while the ^{31}P MAS NMR spectra (Fig. 6b) exhibit compositional evolution associated with progressive depolymerisation of the phosphate network. The ^{7}Li MAS NMR spectra (Fig. 6c) offer complementary insight into the lithium local environments.

The ^{11}B MAS NMR (Fig. 6a) spectra were firstly corrected for the satellite transition contribution and then decomposed using Gaussian model for the signals in $^{[4]}$B region and QMAS 1/2 model for the $^{[3]}$B region using DMFit software [20]. In the ^{11}B MAS NMR spectra, a complex superposition of multiple components within the $^{[4]}$B region was observed, while the [3]B resonance appeared as a single component whose relative intensity increased with higher B_2O_3 content. The decomposition (Fig. 6a, fitting parameters in Table 2) revealed four distinct tetrahedral borate environments ($^{[4]}B_1$–$^{[4]}B_4$), as well as trigonal $^{[3]}$B species. As shown in Fig. 7, the evolution of borate species is presented both in terms of their relative percentages (Fig. 7a) and in terms of the actual number of structural units per formula unit (Fig. 7b). The absolute number of structural units per formula unit was calculated using Equation 1:

$$N_{unit} = \frac{n_{element} \cdot X_{oxide} \cdot P_{unit}}{100}$$

where $n_{element}$ is the number of atoms of interest per mole of the oxide (e.g., 2 for B in B_2O_3), X_{oxide} is the molar fraction of the oxide in the glass, and P_{unit} is the relative proportion of the structural unit (e.g., $^{[4]}B_1$, $^{[4]}B_2$). This converts relative percentages to absolute numbers per formula unit, as illustrated in Fig. 7b. When analysing the evolution of structural units in a glass system, it is valuable to express their abundance not only in relative percentages but also in absolute quantities. This is because absolute values reflect the true number of units present, whereas percentages can be distorted by changes in the overall composition. The dual representation therefore provides a more accurate and nuanced view of the structural transformations occurring within the glass network. In systems like $40Li_2O–20WO_3–(40–x)P_2O_5–xB_2O_3$ where the amount of B_2O_3 varies with each composition, percentage values alone can be misleading. They are influenced by the changing total B_2O_3 content, making it unclear whether an apparent trend results from a genuine structural modification or simply from compositional variation. Expressing the data in absolute numbers eliminates this ambiguity, since these values are independent of the changing B_2O_3 content and thus more faithfully represent the more accurate picture of glass structure evolution.

The observed transformation from $^{[4]}$B to $^{[3]}$B rich glass structures is consistent with trends commonly reported for borophosphate glasses [6,8,21–24]. For $x > 20$, the $^{[3]}$B component becomes predominant, comprising over 50% of total boron species at $x = 25$ and 30.

Since the $^{[4]}$B structural units remain predominant throughout most of the compositional series, particular attention was paid to the evolution of each individual component. The $^{[4]}B_1$ unit, dominant at $x = 5$ (78.2%), rapidly diminishes and is nearly absent at $x = 30$ (1.1%). Meanwhile, $^{[4]}B_2$ reaches its maximum concentration at $x = 10$ and then declines. In contrast, $^{[4]}B_3$ and $^{[4]}B_4$ components grow progressively with composition, indicating the formation of structurally distinct tetrahedral borate environments that emerge only at higher boron levels. This reflects the increasing disorder and structural complexity of the borate subnetwork.

The ^{31}P MAS NMR spectra (Fig. 6b) show broad resonances whose maxima gradually shift towards more positive chemical shift values with increasing B_2O_3 content. This trend again reflects the depolymerisation of phosphate chains through P–O–B substitution, consistent with previous reports [16,25–30]. The parent glass ($x = 0$) spectrum was decomposed using DMFit [20], revealing four components assigned to Q^2, Q^1_{1W}, Q^2_{1W}, and Q^0_{xW} phosphate species, following the Q^n_{mX} nomenclature. Where n = number of connected phosphorus (P) units, mX = number of connected X units, where X represents boron (B) or a transition metal ion (W). The Q^1_{1W} and Q^2 species dominate the parent composition, suggesting a moderately polymerised phosphate

Table 2
^{11}B 1D NMR fitting parameters of $40Li_2O–20WO_3–(40–x)P_2O_5–xB_2O_3$ glass series: assignment, isotropic chemical shift (δ_{iso}, ±0.1 ppm), full width at half maximum (FWHM, ±0.2 ppm), quadrupolar constant (C_Q, ±0.1 MHz), asymmetry parameter (η_Q, ±0.1) and relative proportions (rel. prop., ±1%).

x	$^{[4]}B_x$	δ_{iso}	FWHM	Rel. prop.	$^{[3]}$B	δ_{iso}	C_Q	η_Q	Rel. prop.
mol%		ppm	ppm	%		ppm	MHz	[−]	%
5	$^{[4]}B_1$	−3.3	2.1	78.2					
	$^{[4]}B_2$	−1.0	2.5	21.8					
10	$^{[4]}B_1$	−3.3	1.9	37.9	$^{[3]}$B	+15.7	2.5	0.5	10.3
	$^{[4]}B_2$	−1.1	1.8	34.5					
	$^{[4]}B_3$	+0.1	2.0	15.1					
	$^{[4]}B_4$	+1.3	1.7	2.2					
15	$^{[4]}B_1$	−2.8	2.0	14.4	$^{[3]}$B	+17.5	2.9	0.5	26.7
	$^{[4]}B_2$	−1.0	1.6	19.1					
	$^{[4]}B_3$	+0.0	2.0	35.2					
	$^{[4]}B_4$	+1.9	1.7	4.6					
20	$^{[4]}B_1$	−2.6	2.0	4.5	$^{[3]}$B	+17.9	2.9	0.5	42.1
	$^{[4]}B_2$	−0.9	1.6	10.7					
	$^{[4]}B_3$	+0.2	2.0	36.1					
	$^{[4]}B_4$	+2.0	1.7	6.6					
25	$^{[4]}B_1$	−2.0	2.0	2.0	$^{[3]}$B	+18.0	2.8	0.5	50.6
	$^{[4]}B_2$	−0.5	1.6	7.9					
	$^{[4]}B_3$	+0.5	1.8	29.7					
	$^{[4]}B_4$	+2.0	1.8	9.8					
30	$^{[4]}B_1$	−1.8	1.8	1.1	$^{[3]}$B	+18.2	2.8	0.5	54.4
	$^{[4]}B_2$	−0.3	1.4	6.2					
	$^{[4]}B_3$	+0.7	1.8	30.3					
	$^{[4]}B_4$	+2.1	1.8	8.0					

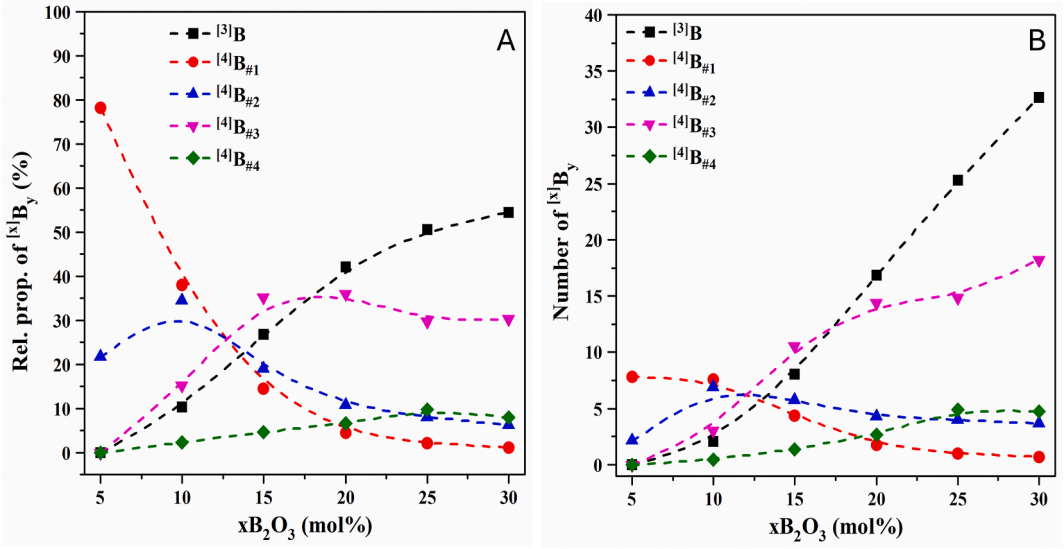

Fig. 7. Evolution of the borate speciation expressed in percentage (a) and in actual number of species (b) versus the B_2O_3 mol% in the $40Li_2O–20WO_3–(40–x)P_2O_5–xB_2O_3$ glasses. The error bars for relative proportions are not shown for clarity (dashed lines are only a guide to the eye).

framework. With increasing B_2O_3 content, the resonances broaden and overlap, impeding reliable decomposition; however, the progressive upfield shift indicates an increasing fraction of less connected phosphate units, such as Q^1 or Q^0, in agreement with the depolymerisation mechanism described above.

The ^{7}Li MAS NMR spectra of the glasses in $40Li_2O–20WO_3–(40–x)P_2O_5–xB_2O_3$ series (Fig. 6c) exhibit a single broad resonance centred close to 0 ppm, whose position and width vary only slightly with composition. For the x = 0 glass, the resonance is observed at −0.79 ppm with a full width at half maximum (FWHM) of 2.94 ppm. With increasing B_2O_3 content, the signal gradually shifts to −0.43 ppm and narrows marginally to a FWHM of 2.69 ppm. The limited chemical-shift variation indicates that lithium ions retain broadly similar ionic oxygen-coordination environments across the entire series. The small downfield shift may reflect subtle changes in average Li–O bonding and second-shell composition associated with the progressive substitution of phosphate by borate units, rather than a change in the fundamental structural role of Li^+. Likewise, the modest linewidth narrowing suggests only a slight reduction in the distribution of local Li environments, consistent with network reorganisation. Overall, the ^{7}Li MAS NMR data indicate that lithium acts primarily as a charge-compensating species associated with non-bridging oxygens or negatively charged network units throughout the series, and do not provide evidence for a pronounced change in Li speciation [31].

Although decomposition of the 1D MAS NMR spectra provided valuable information on the concentration and parameters of the individual components (Table 2), it did not yield insight into their specific nature or connectivity within the borophosphate network. This aspect was further explored using correlation NMR techniques.

3.4.2. *Correlation experiments*

Additional structural insights into the borate and borophosphate network of the $40Li_2O–20WO_3–(40–x)P_2O_5–xB_2O_3$ glass series were obtained using two-dimensional NMR correlation techniques. The formation of B–O–B linkages was investigated via 2D ^{11}B DQ-SQ MAS NMR. The resulting correlation maps are presented in Fig. 8, complemented by horizontal 1D ^{11}B spectra and both 1D and 2D projections.

For the x = 5 sample (Fig. 8a), only the first slice of the 2D experiment, showing the interacting borate species, could be acquired due to the low signal-to-noise. Nevertheless, weak but discernible features corresponding to $^{[4]}B_1$ and $^{[4]}B_2$ structural units can be identified, suggesting the presence of B–O–B connectivity even at low B_2O_3 content. The weak autocorrelation signal of $^{[4]}B_1$ species indicates limited connectivity among these tetrahedral units. However, as the B_2O_3 content increases, no autocorrelation signal for the $^{[4]}B_1$ species can be observed in the 2D DQ-SQ spectra (Fig. 8b–d). This absence indicates that $^{[4]}B_1$ units, whose resonance bands occur between −3.3 to −1.8 ppm, are no longer interconnected via B–O–B bridges but are instead likely engaged in the $B(OP)_4$ species, in agreement with their characteristic chemical shifts [7,8,21–23,32–35].

At higher boron content (x = 10, 20, 30), the 2D DQ-SQ maps show progressively stronger autocorrelation signals in regions attributed to $^{[4]}B_{2\text{-}4}$ species. Interestingly no autocorrelation signal of $^{[3]}$B species can be found at x = 10 but with higher B_2O_3 content x > 10, strong autocorrelation signal of $^{[3]}$B is visible in the spectra, indicating that all present $^{[3]}$B units are at this B_2O_3 concentration diluted into the phosphate network. For x = 20 and 30 (Fig. 8c and **d**), multiple correlation signals emerge, including autocorrelations of $^{[3]}$B units and off-diagonal interactions between $^{[3]}$B and $^{[4]}B_{2\text{-}4}$ species, indicative of increasing boron–boron connectivity within the borate subnetwork as B_2O_3 replaces P_2O_5.

Complementary information regarding the P–O–B connectivity was obtained from 2D ^{11}B (^{31}P) D-HMQC spectra, shown in Fig. 9. These correlation maps are accompanied by corresponding 1D ^{11}B and ^{31}P spectra and respective 2D projections. In the x = 5 sample (Fig. 9a), two cross peaks are detected, corresponding to P–O–$^{[4]}B_1$ and P–O–$^{[4]}B_2$ linkages, implying the participation of tetrahedral boron units in the mixed borophosphate framework.

As B_2O_3 content increases, the appearance of a new signal in the P–O–$^{[3]}$B correlation region can be observed. The position of the signal in the 2D projection indicates that borate units predominantly interact with phosphate units in the Q^2 region. Moreover, the intensity evolution in the 1D versus 2D projections reveals that the signal intensity in the $^{[3]}$B region increasingly diverges between the 1D MAS NMR and 2D D-HMQC projections (Fig. 9b–d). This suggests that a growing proportion of trigonal boron units ($^{[3]}$B) are no longer involved in B–O–P linkages but instead form B–O–B bonds, consistent with the enhanced autocorrelation of $^{[3]}$B species observed in the DQ-SQ maps.

Interestingly, despite these changes in boron coordination preferences, the phosphate species appear structurally non-selective, showing connectivity with all types of boron units, as observed in the broad ^{31}P correlation patterns across all four samples. Thus, the combined 2D NMR analysis confirms the increasing isolation of trigonal borate units and the transformation of $^{[4]}B_1$ to $B(OP)_4$ motifs with rising B_2O_3

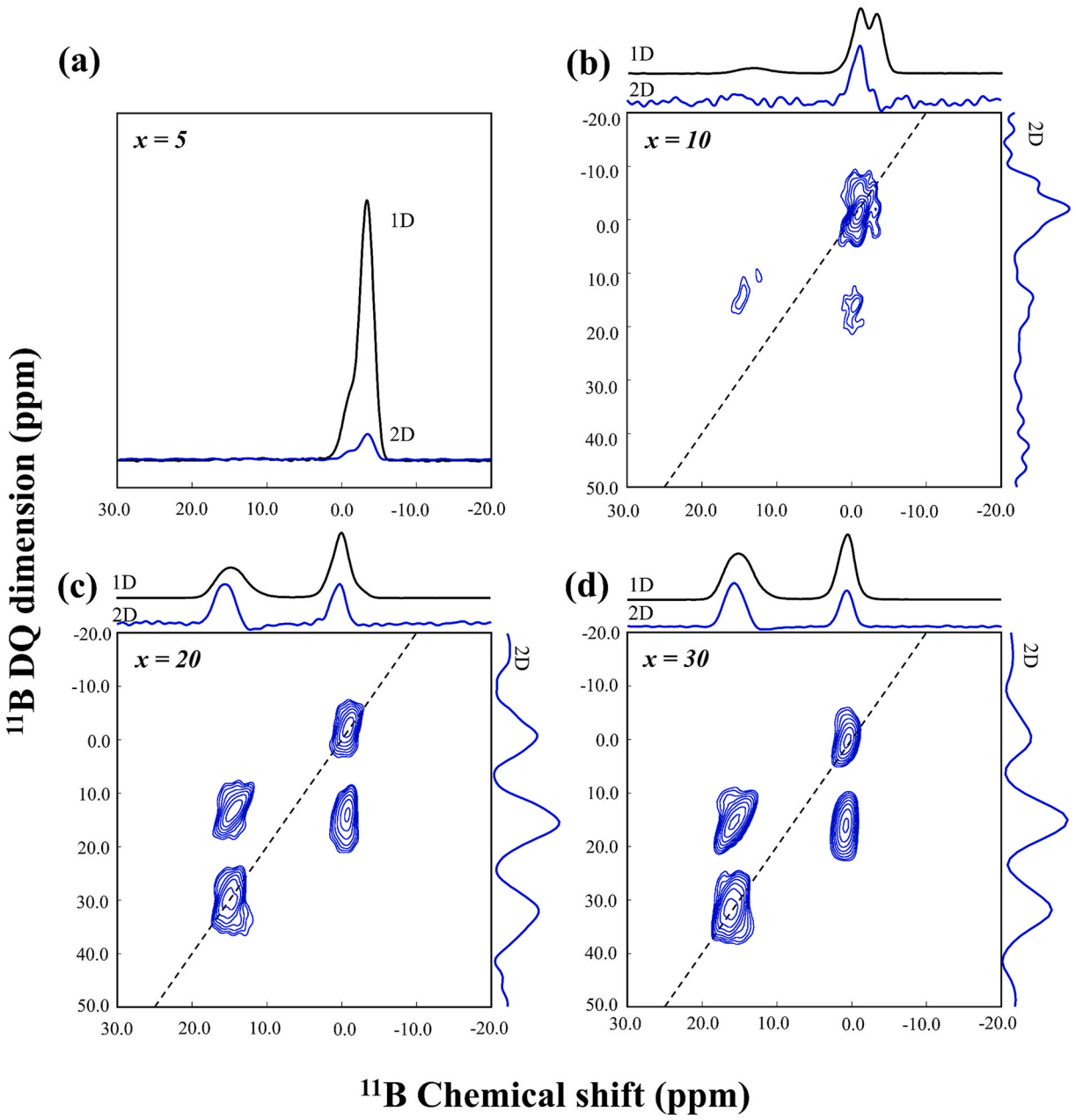

Fig. 8. 1D (x = 5) and 2D ^{11}B DQ-SQ spectra obtained for x = 5 (a), 10 (b), 15 (c) and 30 (d) samples of the $40Li_2O–20WO_3–(40–x)P_2O_5–xB_2O_3$ series. The 2D maps are accompanied with 1D ^{11}B horizontal and ^{11}B 2D horizontal and vertical projections. The dashed diagonal line in each spectrum denotes the $\delta_{DQ} = 2\delta_{SQ}$ auto-correlation region.

content, while phosphate units maintain their structural flexibility and connectivity across the composition series.

To thoroughly evaluate the connectivity within the mixed lithium borophosphate glass network, projections extracted from the 2D ^{11}B (^{31}P) D-HMQC, 2D ^{11}B DQ-SQ correlation spectra, and 1D ^{11}B MAS NMR spectra were compared across samples with B_2O_3 contents of x = 5, 10, 20, and 30 (Fig. 10). This comparison enables the structural role of individual boron species, designated $^{[4]}B_1$ to $^{[4]}B_4$, to be assessed in terms of their participation in P–O–B and B–O–B linkages, as well as their integration within the glass network.

For the sample with x = 5 (Fig. 10a), only a 1D filtered DS-SQ spectrum could be acquired due to a weak NMR signal, attributed to the low boron concentration. Nevertheless, the presence of signals corresponding to interconnected $^{[4]}B_1$ species, along with traces of $^{[4]}B_2$, was still detectable, suggesting the presence of B–O–B connectivity at low B_2O_3 content.

At x = 10 (Fig. 10b), both 2D correlation maps and projections provide a much clearer picture. Here, the structural units $^{[4]}B_2$ and $^{[4]}B_3$ participate in both B–O–B and P–O–B linkages, as evidenced by the cross-peaks in both D-HMQC and DQ-SQ spectra. Interestingly, $^{[4]}B_2$ exhibits a stronger signal in the B–O–B correlation map, while $^{[4]}B_3$ is more dominant in the P–O–B connections. This differentiation implies a functional divergence, where $^{[4]}B_2$ primarily reinforces the borate subnetwork, while $^{[4]}B_3$ acts as a key bridge between borate and phosphate domains. In contrast, $^{[4]}B_4$ is found to participate exclusively in mixed P–O–B linkages, with negligible autocorrelation in the B–O–B map, suggesting that its connectivity is restricted to heteropolar bridging with phosphate units.

This structural tendency is maintained at higher B_2O_3 contents. For x = 20 and x = 30 (Fig. 10c and d), the unit $^{[4]}B_3$ emerges as the principal

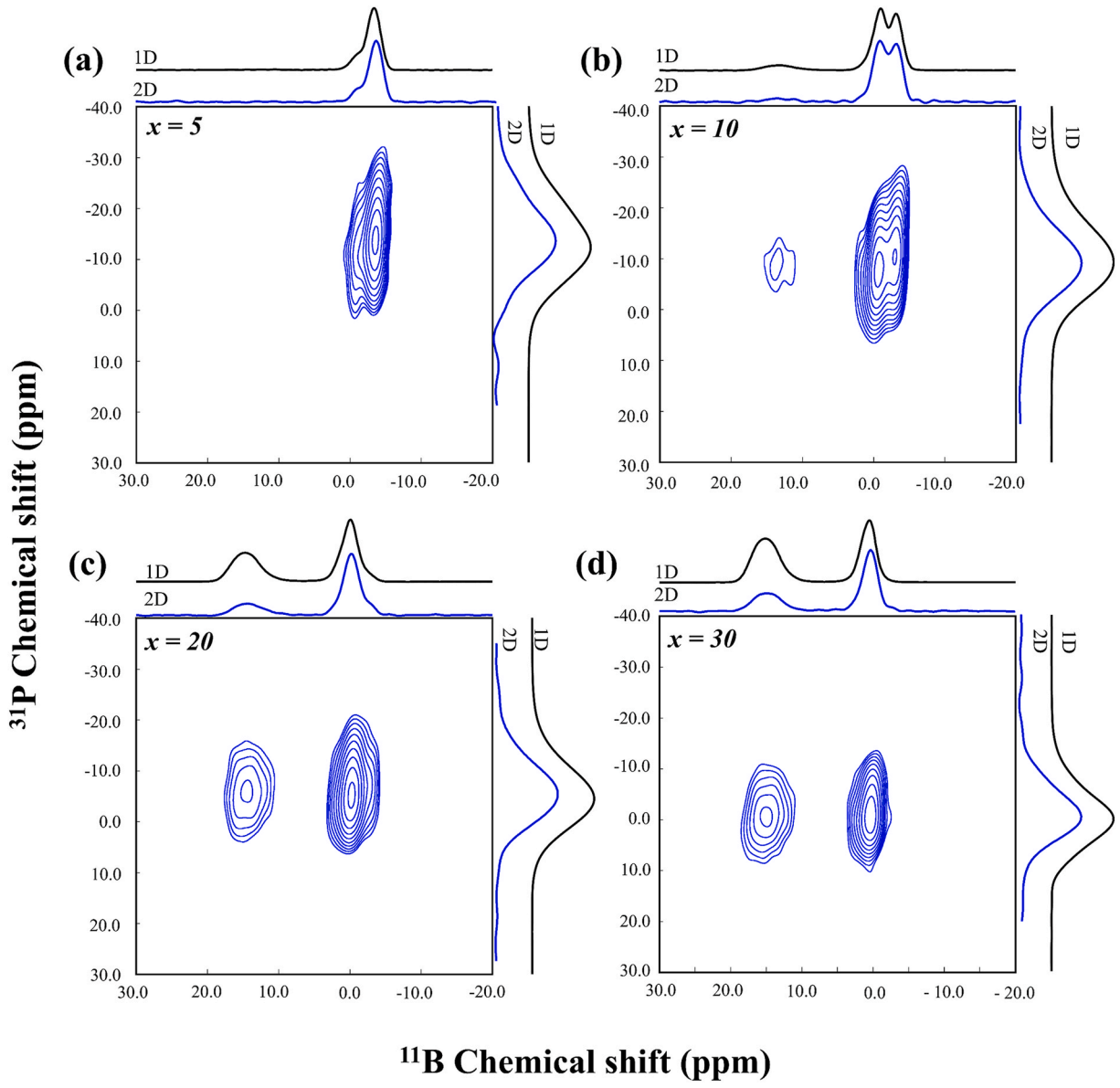

Fig. 9. 2D^{11}B (^{31}P) D-HMQC spectra obtained for x = 5 (a), 10 (b), 15 (c) and 30 (d) samples of the $40Li_2O–20WO_3–(40–x)P_2O_5–xB_2O_3$ series. The 2D maps are accompanied with 1D^{11}B and ^{31}P MAS-NMR spectra and the ^{11}B and ^{31}P 2D projections.

structural motif within the glass network. It shows extensive autocorrelation in the DQ-SQ map and strong cross-peaks in the D-HMQC spectrum, confirming its involvement in all types of linkages: P–O–B, B–O–B, and connections with both trigonal and tetrahedral boron units. This reinforces the interpretation that $^{[4]}B_3$ plays a central role in creating a robust, interconnected borophosphate framework that integrates various boron and phosphate species.

Meanwhile, the $^{[4]}B_1$ unit continues to display behaviour consistent with isolated $B(OP)_4$ motifs. At x = 20, it contributes solely to P–O–B correlations and is absent in B–O–B maps, a pattern that remains unchanged at x = 30.

Overall, the progressive evolution of borate speciation with increasing B_2O_3 content reveals a transition from isolated $^{[4]}B_1$ units to a highly interconnected borophosphate structure dominated by $^{[4]}B_3$ species.

3.4.3. *Borate speciation*

After analysis of the one-dimensional NMR spectra and extraction of information regarding borate structural units from two-dimensional correlation maps, the borate speciation was completed. Through careful spectral decomposition, four distinct boron species were identified in the $^{[4]}$B region and one species in the $^{[3]}$B region. All fitting parameters for the ^{11}B spectra have been compiled in Table 2, and the evolution of each individual component is depicted in Fig. 7.

The ^{11}B chemical shifts are governed not only by coordination number and local bonding topology but also by the nature of the neighbouring cations. Phosphorus, due to its high electronegativity and the formation of localised covalent P–O bonds, contributes to increased shielding and results in more negative chemical shifts for boron in B–O–P environments. In contrast, tungsten, as a heavy transition metal forming polarised W–O bonds with significant d-orbital character, enhances deshielding and shifts the ^{11}B resonance to more positive values in potential B–O–W environments. These trends reflect the relative shielding power of adjacent structural units, which follows the qualitative order: $PO_4 > BO_4 > BO_3 > WO_6$, and on this basis, and combined findings from the NMR analyses (Figs. 6–10), the assignment of borate species is as follows:

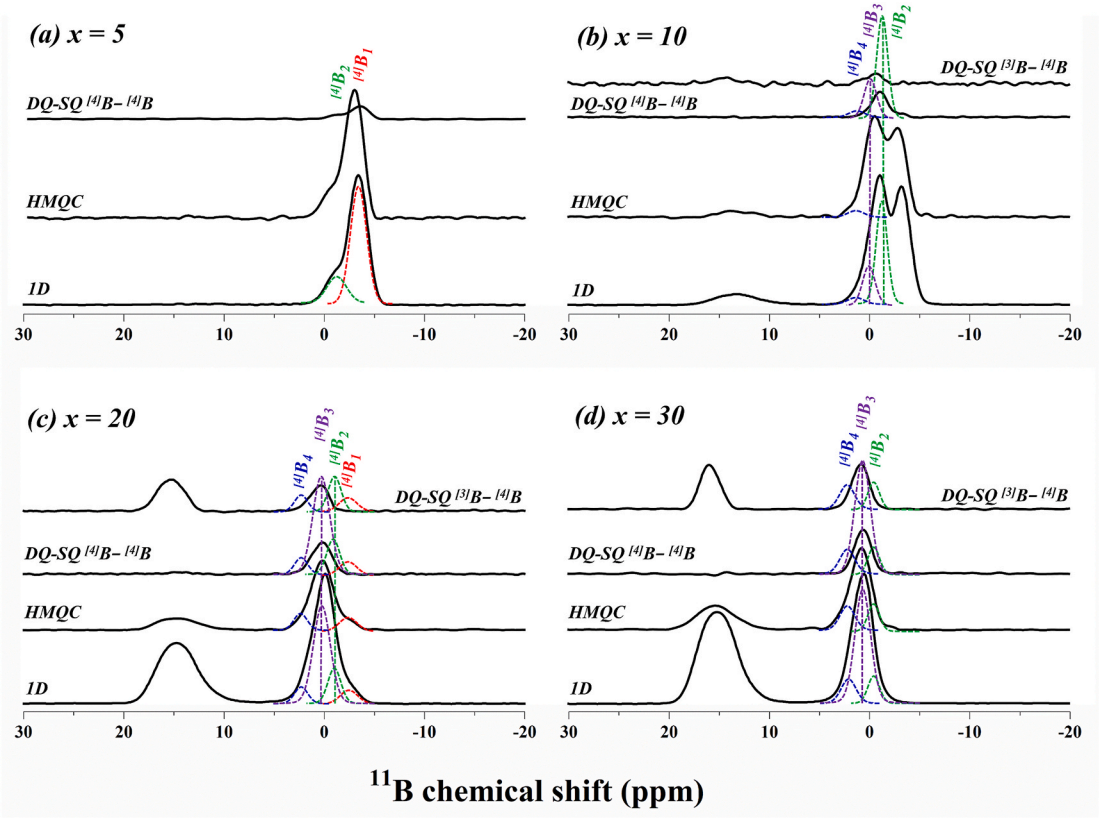

Fig. 10. Comparison of ^{11}B 1D MAS NMR spectra and projections from D-HMQC and DQ–SQ experiments for x = 5 (a), 10 (b), 20 (c) and 30 (d) samples of the $40Li_2O–20WO_3–(40-x)P_2O_5–xB_2O_3$ series, accompanied with components from 1D decomposition highlighting differences between projections.

- The first $^{[4]}$B site, designated as $^{[4]}B_1$, exhibits a chemical shift in the range of −3.3 to −1.8 ppm and is typically attributed to the $B(OP)_4$ structural unit [7,8,21–23,32–35]. However, in the present glass system, the auto-correlation signal observed in the two-dimensional ^{11}B DQ-SQ correlation map at low B_2O_3 content (x = 5) (Figs. 8a and 10a) within the $^{[4]}B_1$ region indicates the presence of $^{[4]}B_1$–O–$^{[4]}B_1$ linkages, consistent with findings in other borophosphate systems [6, 22,23,36–38]. Based on insights from ^{11}B (^{31}P) REDOR experiments on lithium and silver borophosphate glasses [6,36], the $^{[4]}B_1$ species are proposed to correspond to $B(OP)_3(OB)_1$ units at x < 10, and to fully polymerised $B(OP)_4$ units at x > 10.
- The second tetrahedral boron site, designated as $^{[4]}B_2$, exhibits a chemical shift between −1.0 and −0.3 ppm and is involved in almost all possible linkage variations characteristic of the borophosphate glass network. As shown in Fig. 10, this species forms B–O–P and B–O–$^{[4]}$B linkages throughout the entire compositional range starting from the initial additions of B_2O_3. At moderate boron contents, it also clearly contributes to the formation of B–O–$^{[3]}$B linkages, suggesting a versatile role in the formation of both mixed and homonuclear polyhedral connections. However, as the B_2O_3 concentration increases, the participation of the $^{[4]}B_2$ species in B–O–$^{[3]}$B linkages becomes less pronounced, particularly evident in the spectra of samples with the highest B_2O_3 content (Fig. 10c and d). This trend indicates a reduced association of $^{[4]}B_2$ units with trigonal boron sites at high B_2O_3 content. Based on its intermediate chemical shift and considering the hierarchy of chemical shielding, where phosphorus provides the strongest shielding, followed by boron and tungsten, the $^{[4]}B_2$ component can be attributed to boron tetrahedra of the general form $B(OP)_{4-(n+m)}(O^{[4]}B)_n(O^{[3]}B)_m$, where $n = 1$ or 2 and $m = 0$ or 1. This assignment is consistent with earlier studies on structurally similar borophosphate glasses [6,23,24,32–34,37,38] further supporting the interpretation that $^{[4]}B_2$ acts as a fundamental cross-linking unit within the glass network, especially through its bridging between PO_4 and BO_4 tetrahedra.
- The third tetrahedral boron site, designated as $^{[4]}B_3$, exhibits a chemical shift in the range of +0.1 to +0.7 ppm. As illustrated in Fig. 10, this structural unit participates extensively in all available types of borophosphate linkages, including P–O–B, $^{[4]}$B–O–$^{[4]}$B, and particularly $^{[4]}$B–O–$^{[3]}$B. Notably, the $^{[4]}B_3$ species exhibits the strongest presence in the DQ-SQ projections associated with $^{[4]}$B–O–$^{[3]}$B correlations (Fig. 10c and d), making it the dominant contributor to this specific type of connectivity within the glass network. The pronounced signal of $^{[4]}$B–O–$^{[3]}$B in the high-boron-content samples further confirms that $^{[4]}B_3$ assumes a crucial structural role in the B-rich region of the series, complementing the diminishing participation of $^{[4]}B_2$ in such linkages. Considering its more positive chemical shift compared to $^{[4]}B_2$, and applying the established principles of chemical shielding, where the shielding influence follows the order P > B > W, it is inferred that $^{[4]}B_3$ is involved in fewer P–O–B connections and instead favours B–O–B linkages. This chemical environment is thus best described by structural units of the general form $B(OP)_{4-(n+m)}(O^{[4]}B)_n(O^{[3]}B)_m$, where $n + m$ value range from 1 to 4. Consequently, $^{[4]}B_3$ emerges as a key structural species in the formation of a boron-dominated subnetwork within the glass, especially at elevated B_2O_3 contents, where its role in crosslinking between tetrahedral and trigonal boron units becomes structurally significant. Its function thus complements the diminishing role of phosphorus-based connectivity and supports the evolution of the borophosphate network into a mixed B–O–B/P–O–B framework.
- The final tetrahedral boron site, designated as $^{[4]}B_4$, exhibits the most deshielded signal among all $^{[4]}$B components, with a chemical shift in the range of +1.3 to +2.1 ppm. According to Fig. 10, this component participates in the formation of B–O–P linkages, whereas its

involvement in B–O–B linkages is significantly lower, as indicated by the weaker intensity in the DQ–SQ projections compared to $^{[4]}B_2$ and, in particular, $^{[4]}B_3$. The reduced intensity of B–O–B cross-peaks suggests that $^{[4]}B_4$ makes only a minor contribution to borate–borate connectivity within the glass network. At the same time, its distinctly positive chemical shift indicates a local environment that differs from the main borophosphate framework. Considering the relative shielding effects of neighbouring atoms, where phosphorus induces stronger shielding than boron or tungsten, the observed deshielding implies a reduced phosphorus coordination. Although direct spectroscopic evidence for B–O–W linkages cannot be obtained with the present methods, and alternative interpretations such as highly distorted B–O–B environments cannot be fully excluded, the data are consistent with the possible involvement of tungsten in the local coordination of $^{[4]}B_4$. Taking these considerations into account, the $^{[4]}B_4$ species can only be tentatively assigned to structural units of the general type $B(OP)_{4-(n+k)}$ $(O^{[3/4]}B)_n$ $(OW)_k$, where $n = 1$ or 2 and $k = 1$ or 2.

The evolution of borate speciation provides a direct structural basis for the observed mixed glass former effect in the thermal properties. In particular, the concentration dependence of the $^{[4]}B_3$ species closely mirrors the compositional trend of the glass transition temperature. The population of $^{[4]}B_3$ units increases with B_2O_3 addition and reaches a maximum at x = 15, coinciding with the maximum T_g and minimum CTE. This correlation highlights the central role of $^{[4]}B_3$ units in cross-linking the phosphate–borate network through mixed P–O–B and B–O–B connectivities, thereby enhancing network rigidity and thermal stability. At higher B_2O_3 contents ($x \geq 15$), the progressive increase of trigonal $^{[3]}B$ units at the expense of $^{[4]}B_3$ leads to a partial relaxation of the network, reflected by a decrease in T_g and a concomitant increase in CTE. These observations demonstrate that the balance between tetrahedral $^{[4]}B_3$ units and trigonal $^{[3]}B$ species governs the extent of network mixing and non-selectivity, which is a key structural origin of the mixed glass former effect in the thermal behaviour of the studied glasses.

3.4.4. Phosphate speciation

In analogy with the approach adopted for borate speciation, the one-dimensional ^{31}P MAS NMR spectra of the $40Li_2O–20WO_3–(40–x)P_2O_5–xB_2O_3$ glass series were analysed using a physically constrained fitting procedure guided by complementary 2D NMR correlations and literature assignments [24,37–41]. Procedure involves the extraction of phosphorus projections from $2D^{11}B$ (^{31}P) D-HMQC correlation maps (extracted and deconvolved ^{31}P spectral projections are provided in the Supplementary Information). The deconvolution and identification of the parent phosphate and borophosphate glasses were carried out considering previously reported assignments and chemical shift values from the literature [24,37–41], following the previously mentioned Q^n_{mX} nomenclature. All NMR fitting parameters deduced from these decompositions are summarised in Table 3, and representative simulations of the 1D ^{31}P MAS NMR spectra are presented in Fig. 11. The illustration of simplified examples of phosphate, borate-phosphate and tungstate-phosphate species using motifs and colour-coding defined in Ref. [41] are shown in Fig. 12. The proportions of the individual components for samples with x = 0, 5, 10, 20, and 30 are shown both in relative percentages (Fig. 13) and as absolute numbers of species per formula unit (Fig. 14). Due to the time-consuming nature of measuring DQ-SQ and D-HMQC spectra, samples x = 15 and 25 were not measured and therefore decomposition was not possible for these samples (see Fig. 14).

At x = 0, the phosphate network was primarily composed of Q^2 units (−22.7 ppm, 54.8%), which are typically attributed to metaphosphate chains. Minor contributions from Q^2_{1W} (−31.0 ppm, 3.2%), Q^1_{1W} (−12.7 ppm, 39.6%), and $Q^0_{2/3W}$ (−4.0 ppm, 2.4%) were also identified in agreement with previous work [9].

At x = 10, Q^2 units nearly diminished (2.7%), and a broader range of Q^1 and Q^0 species emerged. In particular, Q^0_{3B} units (−6.2 ppm, 16.3%) were now clearly resolved, signifying the formation of isolated orthophosphate groups fully surrounded by three borate units. The presence of Q^1_{1B} and Q^1_{2B} remained substantial (12.4% and 13.4%, respectively), confirming the further depolymerisation of the phosphate sub-network. Meanwhile, the Q^1_{1W} and $Q^0_{2/3W}$ units persisted, although in lower concentrations, indicating the gradual replacement of tungsten by boron as the preferred coordination partner.

In the glass with x = 20, the structural network was almost entirely depolymerised. The Q^2 species were no longer detected, and the spectrum was dominated by Q^1 and Q^0 species. Mixed borophosphate species such as Q^0_{3B} (−6.3 ppm, 29.0%), Q^0_{2B} (0.2 ppm, 16.2%), and Q^1_{1B} (−9.5 ppm, 15.2%) were identified, indicating that most phosphate units now act as isolated, terminal groups surrounded primarily by borate or tungstate units. The Q^1_{2B} species (−18.6 ppm) became negligible (2.6%), showing a continued reduction in the number of phosphate units forming direct bonds with other phosphorus atoms.

At x = 30, the phosphate speciation was dominated by Q^0_{2B} (33.1%), Q^0_{1B} (17.0%), and Q^0_{3B} (16.9%) species. The trend indicates a decrease in the number of borate groups per phosphate unit. This suggests a

Table 3
^{11}P NMR fitting parameters of $40Li_2O–20WO_3–(40–x)P_2O_5–xB_2O_3$ glass series: assignment, isotropic chemical shift (δ_{iso}, ±0.1 ppm), full width at half maximum (FWHM, ±0.2 ppm) and relative proportions (rel. prop., ±1%).

x	Q^n	δ_{iso}	FWHM	Rel. prop.	Q^n_{mW}	δ_{iso}	FWHM	Rel. prop.	Q^n_{mB}	δ_{iso}	FWHM	Rel. prop.
mol%		ppm	ppm	%		ppm	ppm	%		ppm	ppm	%
	Q^n species				Q^n_{mW} species				Q^n_{mB} species			
0	Q^2	−22.7	10.8	54.8	Q^2_{1W}	−31.0	12.5	3.2				
					Q^1_{1W}	−12.7	10.0	39.6				
					$Q^0_{2/3W}$	−4.0	8.0	2.4				
5	Q^2	−22.7	9.3	14.3	Q^2_{1W}	−31.0	8.7	2.1	Q^2_{1B}	−23.4	10.5	4.2
	Q^1	−0.3	7.9	3.4	Q^1_{1W}	−11.9	11.3	47.1	Q^1_{2B}	−16.9	8.8	12.1
					$Q^0_{2/3W}$	−4.8	8.2	7.0	Q^1_{1B}	−9.2	10.1	9.8
10	Q^2	−23.5	8.6	2.7	Q^1_{1W}	−11.6	10.6	32.7	Q^2_{1B}	−24.5	10.5	4.2
	Q^1	+0.4	8.6	7.6	$Q^0_{2/3W}$	−5.0	8.6	10.7	Q^1_{2B}	−16.9	8.7	13.4
									Q^1_{1B}	−10.3	10.1	12.4
									Q^0_{3B}	−6.2	9.3	16.3
20	Q^1	+1.3	8.6	7.6	Q^1_{1W}	−12.3	10.6	8.7	Q^1_{2B}	−18.6	8.7	2.6
	Q^0	+7.3	6.0	2.5	$Q^0_{2/3W}$	−3.7	7.8	18.2	Q^1_{1B}	−9.5	9.8	15.2
									Q^0_{3B}	−6.3	9.3	29.0
									Q^0_{2B}	+0.2	7.2	16.2
30	Q^1	+1.3	8.6	7.3	Q^1_{1W}	−12.8	10.6	3.2	Q^0_{3B}	−6.5	9.2	16.9
	Q^0	+7.9	6.0	5.5	$Q^0_{2/3W}$	−3.6	7.8	17.0	Q^0_{2B}	+0.4	7.3	33.1
									Q^0_{1B}	+4.4	7.7	17.0

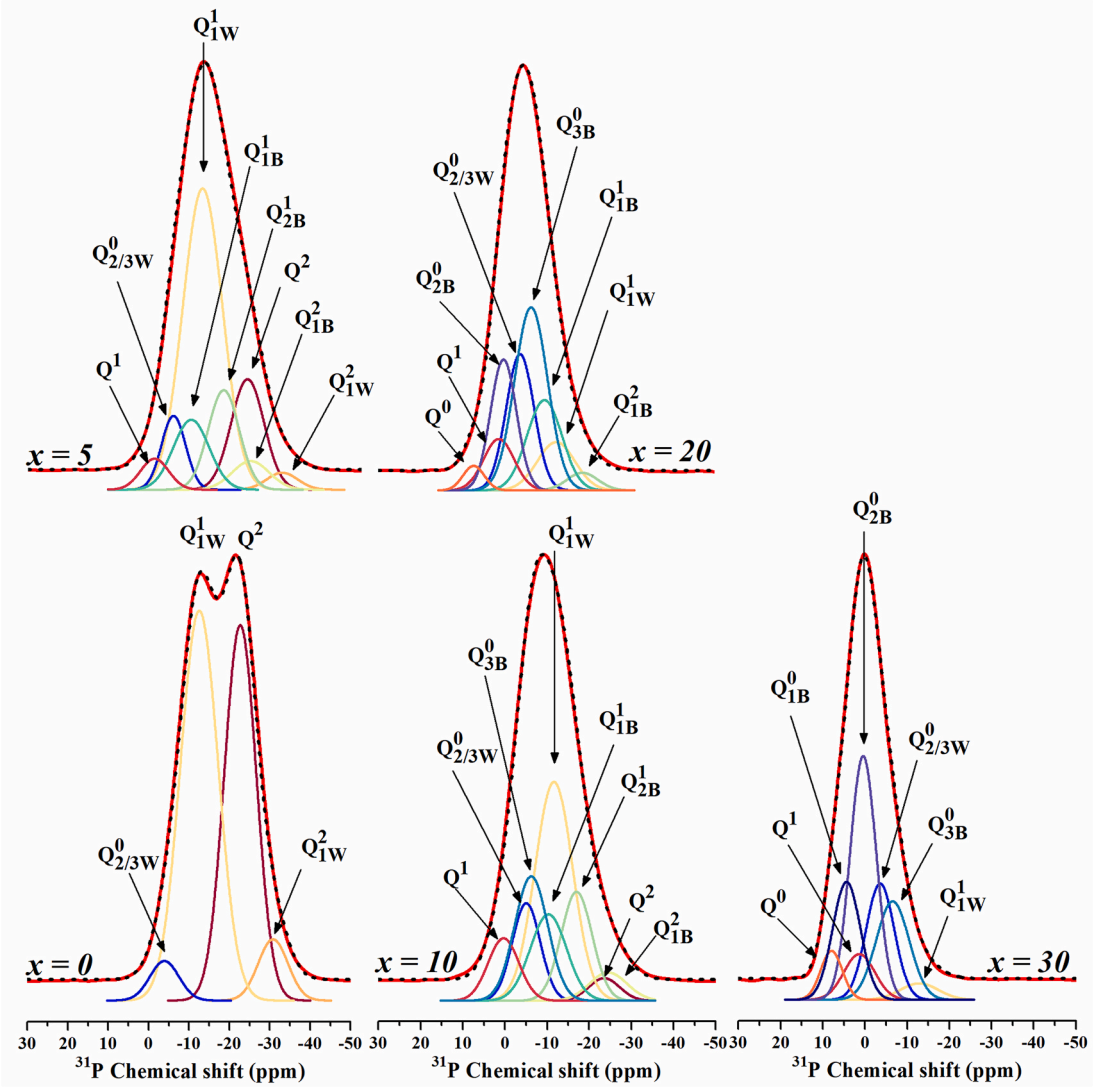

Fig. 11. 1D^{31}P MAS NMR spectra (red line) of samples x = 0, 5, 10, 20 and 30 accompanied with the model (dashed line) and individual components used to decompose the spectra of glasses in the $40Li_2O–20WO_3–(40–x)P_2O_5–xB_2O_3$ system. (For interpretation of the references to colour in this figure legend, the reader is referred to the Web version of this article.)

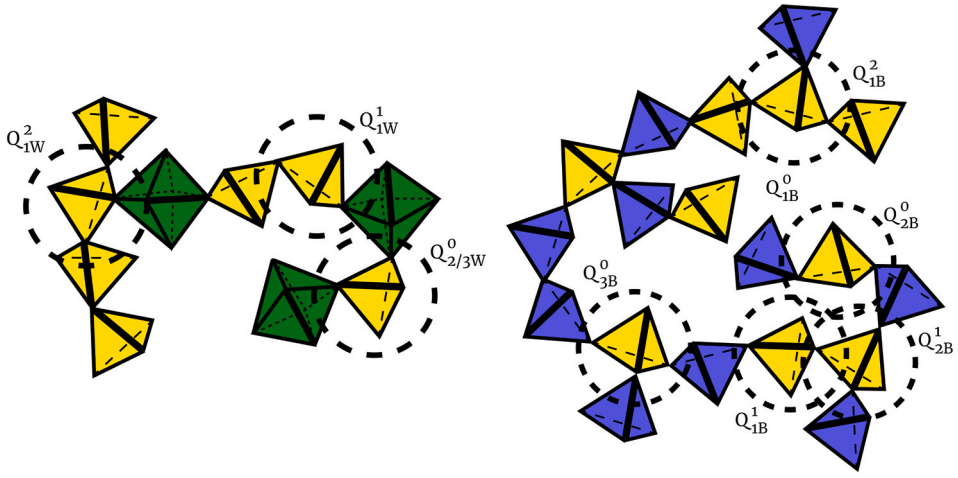

Fig. 12. The illustration of simplified examples of phosphate, borate-phosphate and tungstate-phosphate species occurring in glass structure (blue objects represent BO_4 tetrahedra; yellow objects represent PO_4 tetrahedra; green objects represent WO_6 octahedra). (For interpretation of the references to colour in this figure legend, the reader is referred to the Web version of this article.)

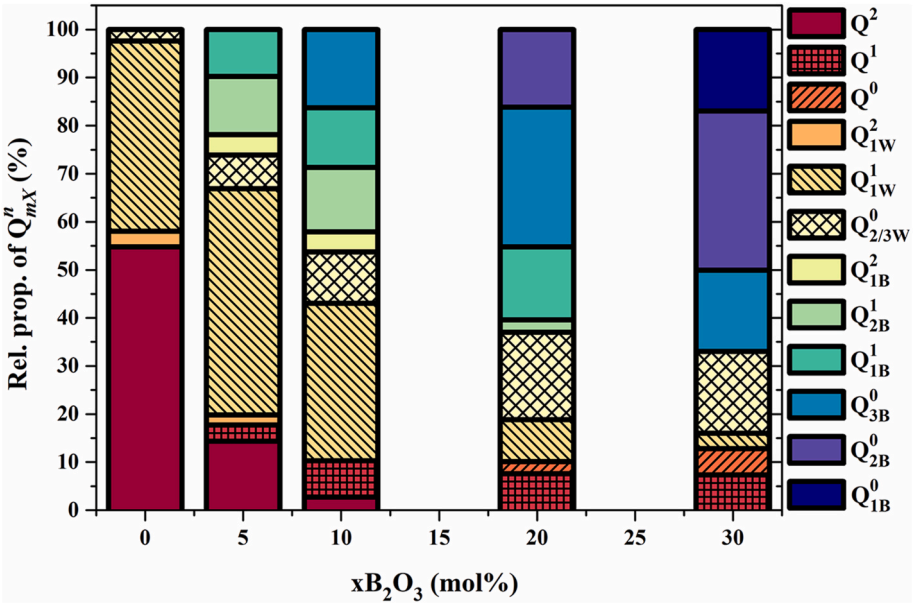

Fig. 13. Evolution of the phosphate speciation expressed in relative percentage versus the B_2O_3 mol% in the $40Li_2O–20WO_3–(40–x)P_2O_5–xB_2O_3$ system. The error bars for relative proportions are not shown for clarity.

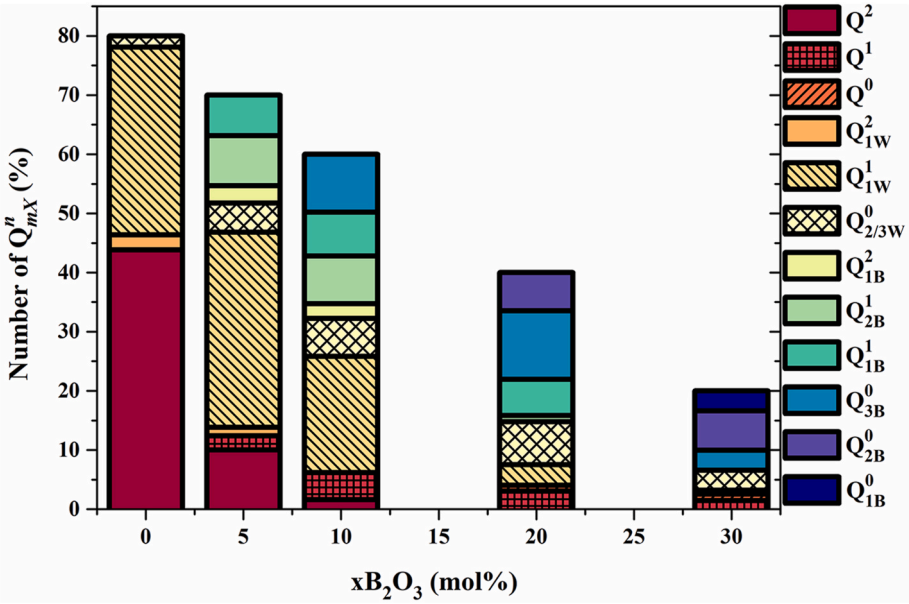

Fig. 14. Evolution of the phosphate speciation expressed in actual number of species per formula unit versus the B_2O_3 mol% in the $40Li_2O–20WO_3–(40–x)P_2O_5–xB_2O_3$ system. The error bars for data are not shown for clarity.

structural reorganisation within the glass network in which borate species begin to preferentially form B–O–B linkages instead of bonding to phosphate units. This interpretation is supported by two-dimensional ^{11}B DQ–SQ NMR, which show increased autocorrelation signals between boron units at higher B_2O_3 contents.

In summary, the addition of B_2O_3 to the lithium phosphate–tungstate glass matrix results in a progressive depolymerisation of the phosphate network. The initial linear and ring phosphate structures (Q^2 and Q^2_{1W}) are gradually substituted by isolated phosphate units (Q^0) coordinated to borate species. The number of borate linkages per phosphate unit decreases at higher B_2O_3 contents as borate species begin to self-connect, forming a borate-rich sub-network. This structural transformation has a profound influence on the connectivity and properties of the glass system and reflects the compositional dependence of phosphate-borate-tungstate interactions.

3.5. EPR spectroscopy

The EPR spectra measured at the temperature of 50 K are shown in Fig. 15a. Two signals (S1 and S2) were observed. The S1 signal appears at the *g* factor $g = 1.918$ while the S2 one has the *g* factor $g = 1.724$. These *g* factor values are typical for W^{5+} [42,43]. Considering the glass compositions including tungsten one may conclude that indeed the W^{5+} ions are present within the glass hosts. Both signals are multicomponent having the features typical for the powder pattern [44] indicating their origin from crystalline particles inside the glass. To prove this and to investigate more the crystallisation processes appearing in the glass hosts depending on the phosphorus content the spectra in Fig. 15a were

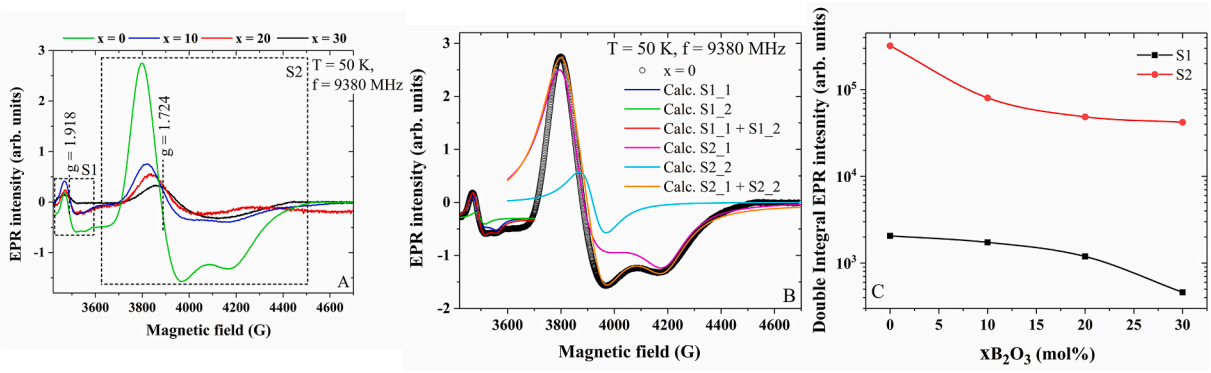

Fig. 15. A – experimental EPR spectra (signals S1 and S2 are indicated by the dashed oblongs) measured at T = 50 K in 4 different samples of $40Li_2O–20WO_3–(40–x)P_2O_5–xB_2O_3$ glass series with different boron content as indicated in the legend. B – experimental spectrum (the most intense one in the sample with 0 mol% boron content) and the calculated ones as indicated in the legend. C – double integral intensity of the S1,2 signals. The connecting line is only eye-guiding.

fitted with the calculated ones using the following spin-Hamiltonian (**Equation 2**):

$$\widehat{\mathbf{H}} = \beta \widehat{\mathbf{S}} \widehat{\mathbf{g}} \mathbf{H}$$

where $\beta, \widehat{\mathbf{S}}, \widehat{\mathbf{g}}, \mathbf{H}$ are Bohr magneton (tabulated constant), vector electron spin operator ($\widehat{\mathbf{S}} = (\widehat{S}_x \ \ \widehat{S}_y \ \ \widehat{S}_z)$), diagonalized g tensor with the components $g_{1,2,3}$, and magnetic field vector, respectively. The experimental and calculated spectra are shown in Fig. 15b on example of the x = 0 mol% B_2O_3 content sample with the phosphorus content of 40 mol% where the intensity and resolution of the S1,2 signals were the largest. Each of the S1,2 signals are composed of two signals – one demonstrates amorphous features possessing isotropic g factor ($g_1 = g_2 = g_3$) while the other one has indeed the axial powder-like properties ($g_1 = g_2 \neq g_3$) [44]. The fit is good proving the correctness of the model. The g tensor components determined for each sample are listed in Table 4. For S1,2 signals, the amorphous signals are designated as S1,2_1 while the axial signals are S1,2_2.

The S1_1,2 signals have the g tensor/factor unchanged upon the changing phosphorus content (**Table 4**). Amorphous S1_2 signal should be produced by the W^{5+} within the glass host, the disordered structure without preferred orientations. The axial S1_1 is the W^{5+} should originate from the place in glass where the crystallisation to a small crystalline nanoparticle below the resolution of XRD (no crystalline phase was detected – see Supporting Information) took place.

In the case of all axial signals the average g factor ($g_{av} = (g_1 + g_2 + g_3)/3$) was calculated and listed in Table 4. The isotropic g factor of the amorphous signals is equal to the average g factor. Comparing the g_{av} of the S1_1 and the isotropic g factor value of the S1_2 one can see that they are practically the same within an error (Table 4). This indicates similar origin of the signals. The W^{5+} ion existing in the crystalline core generates S1_1 signal while the W^{5+} ion originating from the amorphous shell generates S1_2 signal within the core-shell nanostructure. It is worth noting that nanoparticles, in general, grow as core-shell structures [45,46].

Comparing the g_{av} of the S2_1 and the isotropic g factor value of the S2_2 one can see that they are practically the same within an error (Table 4). Therefore, similar relation between the axial and isotropic signal as in the case of the S1 can be observed for the S2 signal indicating similar origin. The W^{5+} ion existing in the crystalline core generates S2_1 signal while the W^{5+} ion originating from the amorphous shell generates S2_2 signal within the core-shell nanostructure.

The g tensor/factor of the S1_1,2 are, in general, much larger as compared to the S2_1,2 signals (Table 4) much closer to the free electron value of the 2.0023 [44]. Tungsten is the transition ion, therefore, the energy levels of W^{5+} are influenced by the symmetry and strength of the local ligand field [42]. The ligand field strength is governed by the W–O distance – the longer it is the weaker the field and oppositely. The weaker field results in the weaker splitting of the energy levels and vice versa. This in turn influences the g tensor/factor values. The spin-orbit coupling constant is negative for the less than half-filled outer shell (W^{5+} has 4 d^1). Mixing of the W^{5+} orbitals with the ligand orbitals leads to the reduction of the spin-orbit coupling. The shorter the W–O bond the stronger the mixing and the reduction of the spin-orbit coupling constant. All these leads to the conclusion that the shorter the W–O bond length the larger the average g tensor or isotropic g factor value. Based on these considerations one may conclude that the S1 signal should originate from the phase with shorter W–O bonding than in the case of the S2 signal. It is known that in tungstates the W^{5+} g factor have values close to the 2.0023 while in the other lattices they are far below the 2.0023 [44]. Therefore, one may conclude that the S1 signal should be produced by WO_3 component of the glass.

In contrast to the S1_1,2 signals, the g tensor/factor of the S2_1,2 signals undergo changes upon the changing B_2O_3 content (Table 4). They are decreasing upon the boron content. Based on the considerations above one may conclude that phosphorus leads to the stabilization of the W^{5+} producing S2 signals in the part of P_2O_5, i.e., substitution of P_2O_5 for B_2O_3 takes place. This can be proven also by the almost three orders of magnitude stronger S2 as compared to the S1. The B_2O_3 content dependences of the double integral intensities of the S1,2 signals (directly proportional to the paramagnetic specie concentration in a host [42]) are shown in Fig. 15c. While the S2 signal intensity is constantly decreasing the S1 signal intensity reaches plateau with considerably less steep decrease upon the B_2O_3 content as compared to the S2. The decrease of the W^{5+} centres upon decreasing phosphorus content is logical. The P^{5+} ions requires compensation of the extra positive charge in the host and obviously the transition ion W^{6+} is reduced to W^{5+}. The lower the phosphorus content the lesser the compensation is needed.

Table 4
The g factor values. The accuracy of determination was ±0.007.

Signal	g_1	g_2	g_3	g_{av}
S1_1 (all samples)	1.927	1.927	1.882	1.912
S1_2 (all samples)	1.916	1.916	1.916	1.916
S2_1 (x = 30)	1.719	1.719	1.600	1.679
S2_2 (x = 30)	1.670	1.670	1.670	1.670
S2_1 (x = 20)	1.730	1.730	1.620	1.693
S2_2 (x = 20)	1.695	1.695	1.695	1.695
S2_1 (x = 10)	1.740	1.740	1.600	1.693
S2_2 (x = 10)	1.700	1.700	1.700	1.700
S2_1 (x = 0)	1.750	1.750	1.600	1.700
S2_2 (x = 0)	1.710	1.710	1.710	1.710

3.6. Electrical properties

The electrical properties of glasses from the series $40Li_2O–20WO_3–(40–x)P_2O_5–xB_2O_3$ were investigated by impedance spectroscopy. Conductivity spectra recorded at different temperatures for representative sample $x = 25$ are displayed in Fig. 16a. The conductivity isotherms for the lithium-based system exhibit the typical features of disordered ionic conductors: a plateau corresponding to the DC conductivity (σ_{DC}), indicative of long-range lithium ion migration, and a dispersive high-frequency region (σ_{AC}) associated with localised hopping of charge carriers. With increasing temperature, the frequency-dependent conductivity shifts towards higher frequencies, consistent with thermally activated ionic motion. The third spectral feature, manifested as a pronounced decrease in conductivity at low frequencies and elevated temperatures, can be attributed to the electrode polarization effect. This phenomenon is commonly associated with the blocking and accumulation of mobile Li^+ ions at the interface of the gold electrodes which serve as electrical contact in present IS measurements. The observation of this effect suggests that ionic charge transport plays a dominant role in the studied glass, which is in good agreement with its composition and expected structural features.

The temperature dependence of σ_{DC} for all compositions follows Arrhenius behaviour (Fig. 16b), and the corresponding activation energies for DC conduction (W_{DC}) were extracted from the slope of log (σ_{DC}·T) versus 1000/T plots, using **Equation 3:**

$$\sigma_{DC}T = \sigma_0 \, exp\left(\frac{-W_{DC}}{k_B T}\right)$$

where σ_0 is the pre-exponential factor, k_B is the Boltzmann constant, and T is the temperature (K). All glasses exhibit excellent linearity with coefficients of determination $R^2 > 0.999$.

The values of σ_{DC} at 30 °C and W_{DC} for each glass composition are summarised in Table 5 and compared graphically in Fig. 17. Here, it should be noted that the DC conductivity values for all glasses were determined directly from the low-frequency conductivity plateau. For selected glasses, Nyquist plots and equivalent-circuit modeling, presented as an example of another approach to determining DC conductivity, are provided in the Supporting Information file. The conductivity values span from 7.20×10^{-9} Ω^{-1} cm^{-1} for the glass with $x = 0$ to 2.49×10^{-7} Ω^{-1} cm^{-1} for the composition with $x = 25$, which is an increase of nearly two orders of magnitude. The corresponding W_{DC} values decrease from 0.67 eV to a minimum of 0.54 eV, showing an inverse correlation with conductivity.

The observed dependence of σ_{DC} on B_2O_3 content exhibits a typical positive mixed glass former effect (MGFE). The initial substitution of P_2O_5 by B_2O_3 enhances σ_{DC} significantly, with the largest increase observed at $x = 10$. Beyond this point the conductivity remains relatively stable, with only a minor variation. A slight decline in σ_{DC} at $x = 30$ is accompanied by a mild increase in W_{DC}, indicating a potential structural rearrangement or onset of less suitable units for ion migration within the glass matrix. Furthermore, the scaling behaviour of the conductivity spectra (see SI, Fig. 5S) along with Nyquist plots (see SI, Figs. 3S and 4S) and strong electrode polarization effect observed in conductivity spectra (see Fig. 16a) suggests that charge transport is studied glasses is governed by a common dominant relaxation mechanism. In view of previous studies on structurally and compositional related alkali tungsten-containing phosphate glasses [9,27,47,48], the

Table 5
The number density of lithium ions, N_V (Li^+), DC conductivity, σ_{DC}, @30 °C, and the activation energy for DC conductivity, W_{DC}, for glasses from series $40Li_2O–20WO_3–(40–x)P_2O_5–xB_2O_3$.

x	N_V (Li^+)	σ_{DC} @30 °C ± 1 %	W_{DC} ±1 %
mol%	10^{22} cm^{-3}	Ω^{-1} cm^{-1}	eV
0	1.39	7.20×10^{-9}	0.67
5	1.44	4.22×10^{-8}	0.62
10	1.51	1.35×10^{-7}	0.58
15	1.54	2.04×10^{-7}	0.56
20	1.61	2.18×10^{-7}	0.56
25	1.67	2.49×10^{-7}	0.54
30	1.70	1.72×10^{-7}	0.56

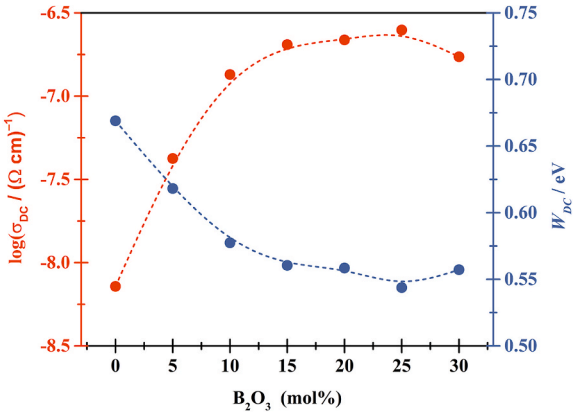

Fig. 17. DC conductivity, σ_{DC}, at 30°C, and activation energy for DC conductivity, W_{DC} for glasses from series $40Li_2O–20WO_3–(40–x)P_2O_5$-$xB_2O_3$.

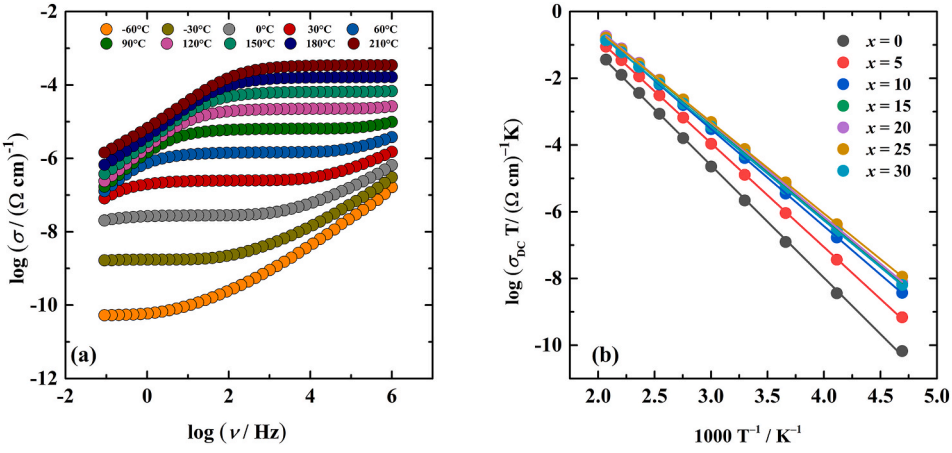

Fig. 16. (a) Conductivity spectra at different temperatures for the $40Li_2O–20WO_3–15P_2O_5–25B_2O_3$ glass, and (b) Arrhenius plots of DC conductivity for glasses from series $40Li_2O–20WO_3–(40–x)P_2O_5–xB_2O_3$. The lines connecting data points in (b) were obtained through linear regression.

present results are consistent with predominantly ionic transport. However, a minor electronic contribution associated with mixed-valance tungsten centres cannot be fully excluded based on performed measurements.

Therefore, given that the number density of Li^+ ions changes only slightly within the series (see Table 5), the conductivity behaviour can be rationalised based on the structural evolution which influences mobility of these ions. According to the results from the MAS NMR spectroscopy at low B_2O_3 concentrations ($x \leq 10$), the phosphate network, initially rich in Q^2 and Q^2_{1W} units, is gradually depolymerised into Q^1 and mixed units such as Q^1_{1W} and $Q^0_{2/3W}$. This depolymerisation results in shorter phosphate chains, which are more effectively cross-linked by tungstate and borate units. Such a configuration may facilitate the formation of interconnected conduction pathways for Li^+ ions. The observed leveling off the conductivity above $x = 10$ corresponds well with this structural transition, suggesting optimal ionic transport occurs when the glass network consists of moderately depolymerised phosphate species and a high degree of network connectivity via mixed structural units. Similar interplay between structural features and transport of Li^+ ions is also observed in the series with higher WO_3 content (series B: $40Li_2O–30WO_3–(30–x)P_2O_5–xB_2O_3$), however the higher conductivity and reduced compositional dependence in Series B arise from the formation of mixed phosphate–tungstate structural units (e.g., W–O–P linkages), which modify network connectivity and provide conduction pathways, rather than from a mere polymerisation effect, see Electrical properties of $40Li_2O–30WO_3–(30–x)P_2O_5–xB_2O_3$ glasses in the Supporting Information.

4. Conclusion

Lithium borophosphate glasses in the compositional range $40Li_2O–20WO_3–(40\text{-}x)P_2O_5–xB_2O_3$ (x = 0–30 mol% B_2O_3) were prepared to systematically investigate the interplay between tungstate modification and mixed glass former effects in lithium-based oxide glasses. By keeping the Li_2O and WO_3 contents constant and selectively substituting $P_2O_5$with B_2O_3, the present compositional design isolated the influence of mixed glass formers on structural organisation, thermal stability, and ionic transport, extending previous studies that were limited to single-former phosphate networks.

Thermal analysis revealed a pronounced mixed glass former effect in the thermal properties, with the glass transition temperature reaching a maximum and the coefficient of thermal expansion reaching a minimum at intermediate B_2O_3 contents (x ≈ 15). Detailed Raman and multi-dimensional MAS NMR analyses established a direct structural origin for this behaviour. In particular, the population of tetrahedral boron units of the $^{[4]}B_3$ type closely mirrors the T_g trend, demonstrating that these units play a central role in cross-linking the phosphate–borate network through mixed P–O–B and B–O–B connectivities. The dominance of $^{[4]}B_3$ at intermediate compositions promotes a highly interconnected, non-selective glass network, which underlies the enhanced thermal stability characteristic of the mixed glass former effect. At higher B_2O_3 contents ($x \geq 15$), the increasing fraction of trigonal $^{[3]}B$ units at the expense of $^{[4]}B_3$ leads to partial network relaxation, manifested by a decrease in T_g and a concomitant increase in CTE.

Electron paramagnetic resonance spectroscopy provided complementary insight into the structural role of tungsten. The detection of W^{5+} centres with distinct amorphous and axial components indicates the presence of tungsten in both fully disordered glass environments and nanoscale, XRD-invisible core–shell-like structural motifs. The systematic decrease of W^{5+} centres associated with phosphorus-rich environments upon increasing B_2O_3 content demonstrates that phosphorus plays a key role in stabilising reduced tungsten species. These results corroborate the NMR-based picture of phosphate–tungstate coupling and show that tungsten remains structurally active within the glass network even as the balance between phosphate and borate formers is varied.

Electrical conductivity measurements confirmed the presence of a positive mixed glass former effect (MGFE), whereby partial substitution of P_2O_5 by B_2O_3 initially enhances dominant ionic conductivity. In these glasses, the percolation of Li^+ conduction pathways is strongly correlated with the evolution of phosphate units speciation and borate coordination. Partial depolymerisation of the phosphate network, together with the formation of mixed phosphate-borate units, particularly borate-tungstate linkages, enhances pathway connectivity and reduces migration barriers, resulting in maximum conductivity at $x = 25$. At higher B_2O_3 concentrations, the increasing B–O–B connectivity and emerging structural segregation diminish pathway continuity, consistent with the slight decrease in conductivity observed experimentally. In contrast, series B exhibited higher conductivity values throughout, achieving a maximum of $6.31 \times 10^{-7}\ \Omega^{-1}\ cm^{-1}$ already at $x = 10$. This improvement is attributed to the higher WO_3 content in Series B, which facilitates more effective modification of the phosphate network connectivity and stabilises WO_6-based conduction pathways.

CRediT authorship contribution statement

Tomáš Hostinský: Writing – review & editing, Writing – original draft, Visualization, Methodology, Investigation, Formal analysis, Data curation, Conceptualization. **Grégory Tricot:** Writing – review & editing, Supervision, Methodology, Investigation, Formal analysis, Data curation. **Ladislav Koudelka:** Writing – review & editing, Writing – original draft, Supervision, Methodology, Conceptualization. **Petr Mošner:** Writing – review & editing, Validation, Supervision, Resources, Methodology, Investigation, Conceptualization. **Lionel Montagne:** Writing – review & editing, Validation, Supervision, Methodology, Investigation, Conceptualization. **Maksym Buryi:** Writing – review & editing, Writing – original draft, Visualization, Methodology, Formal analysis, Data curation. **Andrey Prokhorov:** Visualization, Methodology, Investigation, Data curation. **Marta Razum:** Visualization, Validation, Methodology, Investigation, Formal analysis, Data curation. **Luka Pavić:** Writing – review & editing, Validation, Supervision, Methodology, Investigation, Conceptualization. **Ana Šantić:** Writing – review & editing, Writing – original draft, Validation, Supervision, Methodology, Investigation, Conceptualization.

Declaration of generative AI in scientific writing

During the preparation of this work the author(s) used ChatGPT 5 in order to improve the readability and language of the manuscript. After using this tool/service, the author(s) reviewed and edited the content as needed and take(s) full responsibility for the content of the published article.

Declaration of competing interest

The authors declare that they have no known competing financial interests or personal relationships that could have appeared to influence the work reported in this paper.

Acknowledgements

This work is dedicated to the memory of prof. Ing. Ladislav Koudelka, DrSc., who passed away during the publication process and whose work was fundamental to this study.



Czech authors would like to thank Dr. Helena Drobná for Raman spectra measurements and Dr. L. Benes for the X-ray diffraction measurements. T. Hostinský would like to thank Barrande Fellowship programme for the financial support of his stay at the laboratory of Dr. Grégory Tricot at the University of Lille. The Chevreul Institute (CNRS FR 2638), Ministère de l'Enseignement Supérieur, de la Recherche et de l'Innovation, Hauts-de-France Region and FEDER are also acknowledged for supporting and partially funding this work. L.P. , M.R. and A.Š. acknowledge the support from internal RBI funding scheme ZI-2023 program (KP1-25) through National Recovery and Resilience Plan 2021–2026 (NPOO), funded by the European Union's NextGenerationEU programme.

Appendix A. Supplementary data

Supplementary data to this article can be found online at https://doi.org/10.1016/j.matchemphys.2026.132480.

Data availability

Data will be made available on request.

References

[1] A. Magistris, G. Chiodelli, M. Villa, Lithium borophosphate vitreous electrolytes, J. Power Sources 14 (1) (1985) 87–91, https://doi.org/10.1016/0378-7753(85)88016-2.
[2] Y. Jin, X. Chen, X. Huang, Raman studies of lithium borophosphate glasses, J. Non-Cryst. Solids 112 (1–3) (1989) 147–150, https://doi.org/10.1016/0022-3093(89)90510-3.
[3] S. Lee, J. Kim, D. Shin, Modification of network structure induced by glass former composition and its correlation to the conductivity in lithium borophosphate glass for solid state electrolyte, Solid State Ionics 178 (5–6) (2007) 375–379, https://doi.org/10.1016/j.ssi.2007.01.011.
[4] B.K. Money, K. Hariharan, Glass formation and electrical conductivity studies of melt quenched and mechanically milled 50Li2O: (50−x) P2O5:xB2O3, Solid State Ionics 179 (27–32) (2008) 1273–1277, https://doi.org/10.1016/j.ssi.2007.12.068.
[5] F. Muñoz, L. Montagne, L. Pascual, A. Durán, Composition and structure dependence of the properties of lithium borophosphate glasses showing boron anomaly, J. Non-Cryst. Solids 355 (52) (2009) 2571–2577, https://doi.org/10.1016/j.jnoncrysol.2009.09.013.
[6] B. Raguenet, G. Tricot, G. Silly, M. Ribes, A. Pradel, Revisiting the 'Mixed Glass Former Effect' in ultra-fast quenched borophosphate glasses by advanced 1D/2D solid state NMR, J. Mater. Chem. 21 (44) (2011) 17693–17704, https://doi.org/10.1039/C1JM12350E.
[7] B. Raguenet, G. Tricot, G. Silly, M. Ribes, A. Pradel, The mixed glass former effect in twin-roller quenched lithium borophosphate glasses, Solid State Ionics 208 (2012) 25–30, https://doi.org/10.1016/j.ssi.2011.11.034.
[8] L. Muñoz-Senovilla, G. Tricot, F. Muñoz, Kinetic fragility and structure of lithium borophosphate glasses analysed by 1D/2D NMR, Phys. Chem. Chem. Phys. 19 (34) (2017) 22777–22784, https://doi.org/10.1039/C7CP04171C.
[9] S. Renka, G. Tricot, T. Hostinský, P. Mošner, L. Koudelka, A. Ibrahim, S. Kubuki, Z. Siketić, A. Šantić, Tailoring a glass network structure through addition of transition metal oxides to enhance ionic conductivity in phosphate glasses, Inorg. Chem. 64 (23) (2025) 11412–11425, https://doi.org/10.1021/acs.inorgchem.5c00313.
[10] S.A. Feller, W.J. Dell, P.J. Bray, 10B NMR studies of lithium borate glasses, J. Non-Cryst. Solids 51 (1) (1982) 21–30, https://doi.org/10.1016/0022-3093(82)90186-7.
[11] D. Wang, J. Zhang, D. Zhang, S. Wan, Q. Zhang, D. Sun, S. Yin, Structural investigation of Li2O–B2O3–MoO3 glasses and high-temperature solutions: toward understanding the mechanism of flux-induced growth of lithium triborate crystal, CrystEngComm 15 (2) (2012) 356–364, https://doi.org/10.1039/C2CE26231B.
[12] R.K. Brow, Review: the structure of simple phosphate glasses, J. Non-Cryst. Solids 263–264 (2000) 1–28, https://doi.org/10.1016/S0022-3093(99)00620-1.
[13] X. Li, A. Lu, H. Yang, Structure of ZnO–Fe2O3–P2O5 glasses probed by raman and IR spectroscopy, J. Non-Cryst. Solids 389 (2014) 21–27, https://doi.org/10.1016/j.jnoncrysol.2014.01.051.
[14] S. Marijan, M. Razum, T. Klaser, P. Mošner, L. Koudelka, Ž. Skoko, J. Pisk, L. Pavić, Tailoring structure for improved sodium mobility and electrical properties in V2O5–Nb2O5–P2O5 Glass(Es)-(Ceramics), J. Phys. Chem. Solid. 181 (2023) 111461, https://doi.org/10.1016/j.jpcs.2023.111461.
[15] P. Mošner, O. Kupetska, L. Koudelka, Sodium phosphate glasses modified by MoO3 andWO3, Phys. Chem. Glasses - Eur. J. Glass Sci. Technol. Part B 59 (5) (2018) 213–220, https://doi.org/10.13036/17533562.59.5.020.
[16] C. C. de Araujo, W. Strojek, L. Zhang, H. Eckert, G. Poirier, S.J.L. Ribeiro, Y. Messaddeq, Structural studies of NaPO3–WO3 glasses by solid state NMR and Raman spectroscopy, J. Mater. Chem. 16 (32) (2006) 3277–3284, https://doi.org/10.1039/B605971F.
[17] I.J. Hidi, G. Melinte, R. Stefan, M. Bindea, L. Baia, The study of the structure and bioactivity of the B2O3 • Na2O • P2O5 system, J. Raman Spectrosc. 44 (8) (2013) 1187–1194, https://doi.org/10.1002/jrs.4330.
[18] A. Moguš-Milanković, K. Sklepić, H. Blažanović, P. Mošner, M. Vorokhta, L. Koudelka, Influence of germanium oxide addition on the electrical properties of Li2O–B2O3–P2O5 glasses, J. Power Sources 242 (2013) 91–98, https://doi.org/10.1016/j.jpowsour.2013.05.068.
[19] P.T. Freudenberger, R.L. Blatt, R.E. Youngman, R.K. Brow, Network structures and the properties of na-ca-sr-borophosphate glasses, J. Non-Cryst. Solids 600 (2023) 121966, https://doi.org/10.1016/j.jnoncrysol.2022.121966.
[20] D. Massiot, F. Fayon, M. Capron, I. King, S. Le Calvé, B. Alonso, J. Durand, B. Bujoli, Z. Gan, G. Hoatson, Modelling one- and two-dimensional solid-state NMR spectra, Magn. Reson. Chem. 40 (1) (2002) 70–76, https://doi.org/10.1002/mrc.984.
[21] L. Koudelka, J. Pospíšil, P. Mošner, L. Montagne, L. Delevoye, Structure and properties of potassium Niobato-Borophosphate glasses, J. Non-Cryst. Solids 354 (2) (2008) 129–133, https://doi.org/10.1016/j.jnoncrysol.2007.07.030.
[22] A. Saitoh, G. Tricot, P. Rajbhandari, S. Anan, H. Takebe, Effect of B2O3/P2O5 substitution on the properties and structure of tin boro-phosphate glasses, Mater. Chem. Phys. 149–150 (2015) 648–656, https://doi.org/10.1016/j.matchemphys.2014.11.021.
[23] M. Zeyer-Düsterer, L. Montagne, G. Palavit, C. Jäger, Combined 17O NMR and 11B–31P double resonance NMR studies of sodium borophosphate glasses, Solid State Nucl. Magn. Reson. 27 (1) (2005) 50–64, https://doi.org/10.1016/j.ssnmr.2004.06.009.
[24] B. Doumert, F. Lecomte, G. Tricot, Advanced solid state 1D/2D NMR investigation of the B2O3-Zn(PO3)2 glasses, J. Non-Cryst. Solids 548 (2020) 120325, https://doi.org/10.1016/j.jnoncrysol.2020.120325.
[25] P. Mustarelli, The nmr information on phosphate glasses: a review, Phosphorus Res. Bullet. 10 (1999) 25–36, https://doi.org/10.3363/prb1992.10.0_25.
[26] S.H. Santagneli, C.C. de Araujo, W. Strojek, H. Eckert, G. Poirier, S.J.L. Ribeiro, Y. Messaddeq, Structural studies of NaPO3−MoO3 glasses by solid-state nuclear magnetic resonance and Raman spectroscopy, J. Phys. Chem. B 111 (34) (2007) 10109–10117, https://doi.org/10.1021/jp072883n.
[27] S. Renka, L. Pavić, G. Tricot, P. Mošner, L. Koudelka, A. Moguš-Milanković, A. A. Šantić, Significant enhancement of sodium ion conductivity in phosphate glasses by addition of WO3 and MoO3: the effect of mixed conventional–conditional glass-forming oxides, Phys. Chem. Chem. Phys. 23 (16) (2021) 9761–9772, https://doi.org/10.1039/D1CP00498K.
[28] K. Bodiang, L. Delevoye, R. Podor, F.O. Méar, Role of molybdenum on the structure and properties of A2O-P2O5−MoO3 (A = Na, Ag, Rb, cs) glasses, J. Non-Cryst. Solids 606 (2023) 122193, https://doi.org/10.1016/j.jnoncrysol.2023.122193.
[29] G. Tricot, K. Ben Tayeb, L. Koudelka, P. Mosner, H. Vezin, Insertion of MoO3 in borophosphate glasses investigated by magnetic resonance spectroscopies, J. Phys. Chem. C 120 (17) (2016) 9443–9452, https://doi.org/10.1021/acs.jpcc.6b02502.
[30] V.A. Adhwaryu, D.K. Kanchan, Ag+ ion conduction in AgI- Ag2O-B2O3-P2O5 glass electrolyte, Mater. Sci. Eng., B 263 (2021) 114857, https://doi.org/10.1016/j.mseb.2020.114857.
[31] H. Bradtmüller, Q. Zheng, A. Gaddam, H. Eckert, E.D. Zanotto, Structural impact of niobium oxide on lithium silicate glasses: results from advanced interaction-selective solid-state nuclear magnetic resonance and Raman spectroscopy, Acta Mater. 255 (2023) 119061, https://doi.org/10.1016/j.actamat.2023.119061.
[32] L. Koudelka, P. Kalenda, P. Mošner, Z. Černošek, L. Montagne, B. Revel, Structural investigation of BaO-B2O3-P2O5 glasses by NMR and Raman spectroscopy, J. Mol. Struct. 1119 (2016) 212–219, https://doi.org/10.1016/j.molstruc.2016.04.066.
[33] H. Takebe, T. Harada, M. Kuwabara, Effect of B2O3 addition on the thermal properties and density of barium phosphate glasses, J. Non-Cryst. Solids 352 (6) (2006) 709–713, https://doi.org/10.1016/j.jnoncrysol.2005.11.066.
[34] D. Zielniok, C. Cramer, H. Eckert, Structure/property correlations in ion-conducting mixed-network former glasses: solid-state NMR studies of the system Na2O−B2O3−P2O5, Chem. Mater. 19 (13) (2007) 3162–3170, https://doi.org/10.1021/cm0628092.
[35] M. Villa, K.R. Carduner, G. Chiodelli, A 31P-NMR study of borophosphate glasses, J. Solid State Chem. 69 (1) (1987) 19–23, https://doi.org/10.1016/0022-4596(87)90004-1.
[36] S. Elbers, W. Strojek, L. Koudelka, H. Eckert, Site Connectivities in Silver Borophosphate Glasses: New Results from 11B{31P} and 31P{11B} Rotational Echo Double Resonance NMR Spectroscopy, Solid State Nucl. Magn. Reson. 27 (1) (2005) 65–76, https://doi.org/10.1016/j.ssnmr.2004.08.007.
[37] G. Tricot, A. Saitoh, H. Takebe, Intermediate length scale organisation in tin borophosphate glasses: new insights from high field correlation NMR, Phys. Chem. Chem. Phys. 17 (44) (2015) 29531–29540, https://doi.org/10.1039/C5CP02095F.
[38] Y. Watanabe, K. Hayashi, G. Tricot, B. Doumert, A. Saitoh, Structural insights into properties of SnO–P2O5–B2O3 glasses: P2O5/B2O3 substitution effect, Mater. Chem. Phys. 323 (2024) 129641, https://doi.org/10.1016/j.matchemphys.2024.129641.
[39] G. Tricot, Mixed network phosphate glasses: seeing beyond the 1D 31P MAS-NMR spectra with 2D X/31P NMR correlation maps, in: G.A. Webb (Ed.), Annual Reports on NMR Spectroscopy, vol. 96, Academic Press, 2019, pp. 35–75, https://doi.org/10.1016/bs.arnmr.2018.08.003.
[40] G. Tricot, L. Alpysbay, B. Doumert, Solid state NMR: a powerful tool for the characterization of borophosphate glasses, Molecules 25 (2) (2020) 428, https://doi.org/10.3390/molecules25020428.
[41] T. Hostinský, L. Koudelka, P. Mošner, G. Tricot, H. Drobná, M. Razum, A. Šantić, The influence of B2O3 on structure and ionic conductivity of lithium phosphate-

niobate glasses, J. Non-Cryst. Solids 646 (2024) 123258, https://doi.org/10.1016/j.jnoncrysol.2024.123258.
[42] C.P. Poole, H.A. Farach, Handbook of Electron Spin Resonance. 2, American Inst. of Physics, New York, 1999.
[43] V.V. Laguta, M. Buryi, M. Nikl, J. Rosa, S. Zazubovich, Hole capture in PbWO 4 : Mo,La(Y) Scintillator crystals, Phys. Rev. B 83 (9) (2011) 094123, https://doi.org/10.1103/PhysRevB.83.094123.
[44] A. Abragam, B. Bleaney, Electron Paramagnetic Resonance of Transition Ions, Oxford Univ. Press, Oxford, 2013. Repr.; The international series of monographs on physics.
[45] M. Buryi, Z. Remeš, V. Babin, A. Artemenko, S. Chertopalov, J. Mičová, Cold plasma treatment of ZnO:Er Nano- and microrods: the effect on luminescence and defects creation, J. Alloys Compd. 895 (2022) 162671, https://doi.org/10.1016/j.jallcom.2021.162671.
[46] L. Procházková, V. Vaněček, V. Čuba, R. Pjatkan, R. Martinez-Turtos, I. Jakubec, M. Buryi, S. Omelkov, E. Auffray, P. Lecoq, E. Mihóková, M. Nikl, Core–shell ZnO: Ga-SiO2 nanocrystals: limiting particle agglomeration and increasing luminescence via surface defect passivation, RSC Adv. 9 (50) (2019) 28946–28952, https://doi.org/10.1039/C9RA04421C.
[47] L. Pavić, A. Šantić, J. Nikolić, P. Mošner, L. Koudelka, D. Pajić, A. Moguš-Milanković, Nature of mixed electrical transport in Ag2O–ZnO–P2O5 glasses containing WO_3 and MoO_3, Electrochim. Acta 276 (2018) 434–445, https://doi.org/10.1016/j.electacta.2018.04.029, 2018.
[48] A. Šantić, J. Nikolić, L. Pavić, R.D. Banhatti, P. Mošner, L. Koudelka, A. Moguš-Milanković, Scaling features of conductivity spectra reveal complexities in ionic, polaronic and mixed ionic-polaronic conduction in phosphate glasses, Acta Mater. 175 (2018) 46–54, https://doi.org/10.1016/j.actamat.2019.05.067.